Advancements in Saturation Transfer Imaging of the Spinal Cord

By

Richard Dylan Lawless

Master's Thesis

Submitted to the Faculty of the

Graduate School of Vanderbilt University

in partial fulfillment of the requirements

for the degree of

MASTER OF SCIENCE

in

Biomedical Engineering

December 12, 2020

Approved:

Seth A. Smith

John Gore

ACKNOWLEDGEMENTS

I would like to acknowledge and thank the sources of funding for this project: Conrad Hilton Foundation (SAS), National MS Society (SAS), NIH/NINDS 1R01NS109114-01 (SAS), and NIBIB T32EB021937. I would also like to express my deep and sincere gratitude to my advisor, Dr. Seth A. Smith, for his constant support in both my research and personal life, and for the invaluable wisdom he has shared with me along the way. I will always be in awe of his empathy, kindness, and devotion to his work. I would also like to thank Dr. Michael Miga, for teaching me the intricacies of scientific writing and for providing me with some of the most memorable opportunities of my life.

I am extremely grateful to my mother, Norma, for the sacrifices she made in preparing me for my future and instilling in me a passion for education. And, lastly, to my loving and supportive partner, Kaitlin, for patiently listening to hours of practice talks. Without her encouragement, none of this would have been possible.

TABLE OF CONTENTS

Page

LIST OF TABLES

LIST OF FIGURES

SPECIFIC AIMS

The spinal cord is a narrow, cylindrical structure responsible for rapidly transmitting electrical signals throughout the nervous system and is the primary sensorimotor pathway for the human body. Therefore, damage to the spinal cord caused by neurodegenerative diseases, such as multiple sclerosis (MS), can lead to severely impaired neurological function. Conventional magnetic resonance imaging (MRI) is sensitive to late-stage inflammatory lesions and tissue atrophy, but are often poor indicators of disease progression and do not report on underlying pathophysiology of MS. Quantitative MRI biomarkers capable of detecting tissue changes earlier in the disease pathology may have significant implications in the diagnosis, prognosis, and treatment of MS.

The primary focus of this work is saturation transfer (ST) imaging, including both quantitative magnetization transfer (qMT) and chemical exchange saturation transfer (CEST). In a ST experiment, a pool of exchangeable protons is saturated using an off-resonance RF pulse, and through direct chemical exchange (CEST) and dipolar coupling (MT) the magnetization is transferred to the surrounding water protons, resulting in an observable attenuation of the water signal. The magnitude of signal attenuation provides an indirect measurement of the exchanging species, which is related to its concentration and exchange rate. The ability to observe and measure the biochemical alterations within tissue provides a distinct advantage over T1- and T2-weighted MRI, which measures water content only, and may help to resolve the disconnect between radiological findings and clinical presentation.

qMT provides quantitative estimates of the semi-solid concentration within tissue, primarily the pool-size-ratio (PSR) which has been shown to correlate with white matter myelin density. CEST, conversely, is a more spectrally selective saturation transfer method that provides sensitivity to endogenous mobile solutes with exchangeable protons. While Amide Proton Transfer (APT), the most commonly explored CEST effect, can be related to protein concentration and pH *in vivo*, it also suffers from several confounding factors. Contributions from larger concentration pools, such as direct water saturation (DS) and the macromolecular (MT) component, often obfuscate the lower concentration metabolite pools which is the target of CEST experiments and may offer greater insight into pathology. Additionally, due to the lack

of a well-established quantitative model, CEST results in the literature are primarily reported by calculating the asymmetry of the CEST Z-spectrum around the amide resonance frequency. This technique is susceptible to changes in the semi-solid pool size as well as relaxation time differences and is dependent on scan parameters, leading to difficulties in reproducibility and limited multisite comparison. Thus, the studies proposed herein will seek to develop a standardized, quantitative technique for modelling the results of CEST experiments in order to extract more specific, clinically relevant information.

Both myelin density and protein/peptide concentration can be aberrant in patients with MS because MS is both a demyelinating and inflammatory process, respectively. Additionally, treatment of neurodegenerative disorders such as MS will alter the chemical composition of the tissue well before any structural changes can be observed with clinical MRI. However, it has not yet been explored how combining the molecular information gained from qMT and CEST experiments can further our understanding of MS pathology, evolution or therapeutic intervention. Therefore, we performed a longitudinal, cross-cohort study of MS patients with varying disease severity within a low-severity cohort to determine if qMT and CEST parameters can act as biomarkers for disease progression and treatment efficacy. We have investigated our hypothesis in both ordered (spinal cord) and disordered (cerebrospinal fluid) tissues to gain a more complete understanding of MS pathology and, ultimately hope the work herein will improve the diagnostic and prognostic capabilities of MRI *in vivo*, closing the gap between radiological imaging and neurological disability.

<u>Aim 1:</u> Develop improved modelling and fitting techniques for assessing Chemical Exchange Saturation Transfer indices.

<u>Hypothesis:</u> Improved quantification of CEST spectra and providing output indices using Z spectral fitting and exchange-based models, we will deconvolve overlapping signals and improve sensitivity to amide proton signals.

CEST imaging is capable of detecting low concentration, endogenous solutes with exchangeable protons groups, however, parsing out specific biochemical contributions to the CEST z-spectrum has proven difficult. Competing effects from direct water saturation, magnetization transfer,

and nuclear Overhauser enhancement often confound the results of semi-quantitative techniques such as MT asymmetry. The goal of this aim is to quantify CEST experiments using Z spectral fitting and informed exchange models to improve the sensitivity, specificity, and repeatability of amide proton transfer (APT) CEST, while reducing the dependence on specific scan parameters.

<u>Aim 2:</u> Evaluate the sensitivity of saturation transfer experiments to pathological changes of both ordered (Aim 2a) and disordered (Aim 2b) tissues in patients with Multiple Sclerosis.
<u>Hypothesis</u>: Indices derived from quantitative saturation transfer experiments will provide more specific biochemical information that can be related to the progression and severity of tissue damage in vivo*.*

Quantitative values extracted from MR images offer a rich framework to understand and evaluate the biochemical composition of both ordered (i.e. spinal cord) and disordered tissues (i.e. cerebrospinal fluid). Therapeutic interventions applied to neurodegenerative disorders can result in altered chemical composition before structural changes are observed. Thus, the ability of saturation transfer techniques to detect alterations in endogenous biochemical substrates can be exploited to provide biomarkers for disease progression and monitoring the efficacy of treatment. By assessing changes in derived, quantitative radiological outputs across cohorts and over time (longitudinal analyses), we can offer unique insight into the substrates of neurological disfunction and new opportunities to assess treatment impact.

SIGNIFICANCE

The spinal cord (SC) is a narrow cylindrical bundle of nerves that plays an essential role in the central nervous system (CNS), acting as the primary sensorimotor pathway to and from the brain. The SC is a clinically eloquent structure, thus, small disruptions, such as the formation of lesions in multiple sclerosis (MS), can lead to substantial neurological deficits. Evidence suggests that damage to the SC drives the continued deterioration of clinical deficits seen in MS patients[1]. Due to the small size of the SC, a 3 mm lesion would be the equivalent of a 40 mm brain lesion and could potentially result in the loss of function of an entire column of white matter (WM).

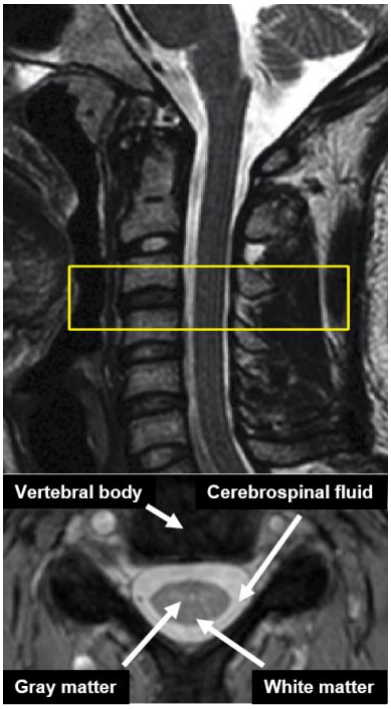

Figure 1. *(Top) Sagittal view of the cervical spinal cord. Yellow box indicates the region of interest, centered on the C3/C4 vertebrae. (Bottom) Axial view of spinal cord indicating major anatomical regions and sources of artifacts and field inhomogeneity.*

Despite the link to MS and other CNS diseases, few quantitative radiological techniques focus on the SC due to the problems associated with acquiring data in such a challenging environment (**Figure 1**). These problems include the size of the SC, which is approximately 15 mm at C3 vertebrae, providing a low signal-to-noise ratio (SNR). The SC sits within large bones which induce a static B0 field inhomogeneity. The proximity to the lungs introduces respiratory motion as well as a temporally varying B0 field leading to non-static field inhomogeneity. The cord is also surrounded by pulsating cerebrospinal fluid (CSF) which can cause motion artifacts. Finally, similar relaxation times across gray matter (GM) and WM in the SC leads to poor intra-cord contrast in clinical scans. Nevertheless, our lab has had many successes in developing quantitative MRI for the SC[2–4]. Herein, I will continue to build upon the foundation laid by our previous work while identifying novel methods to improve quantitative saturation transfer imaging in the SC.

Regarding MS, contrast between lesion and surrounding SC structures are often difficult to appreciate. Further, identifying lesions only demonstrates a late stage manifestation of the

complex progression of MS leading to lesion formation. Conventional MRI is insensitive to the biochemical changes which precede the formation "lesions". In MS, an autoimmune disorder, inflammatory cells and macrophages accumulate in the affected tissue and attack the axon and myelin sheath surrounding WM axons. This process leads to demyelination, axonal damage, and, eventually, to tissue loss and gross inflammation – the formation of lesions detectable by clinical MRI. We hypothesize that the lack of sensitivity to early, sub-voxel, microscopic and biochemical changes has driven the poor correlation between radiologically detected lesions and clinical disability in the literature[5].

In the work presented here, we applied two quantitative MRI techniques: chemical exchange saturation transfer (CEST) and quantitative magnetization transfer (qMT), sensitive to the biochemical and macromolecular components of SC tissue damage in MS, respectively. Both methods rely on saturation transfer, that is, the transfer of spin information between the solute of interest and the surrounding water. CEST provides information about endogenous mobile solutes, typically reflective of neurochemicals/proteins/peptides, and amide proton transfer (APT), the most commonly reported CEST index, has shown to relate to protein concentration and pH in vivo[6]. *We hypothesize that CEST may be sensitive to the influx of inflammatory cells that occurs prior to lesion formation in MS, potentially providing a biomarker for predicting relapse or identifying at-risk tissue for targeted treatment.* Alternatively, qMT provides information about semi-solid components within tissue, typically dominated by myelin, and is characterized by the pool-size-ratio (PSR) which has been demonstrated to correlate well with WM myelin density[7]. *We hypothesize that the PSR can detect the earliest stages of demyelination in the SC, again, prior to lesion formation*. The intent of this research was not only to examine what information can be gained from these methods separately, but how combining the two can provide greater insight to the underlying pathological processes and improved quantitative robustness than either method would alone.

There are a number of challenges in developing quantitative MRI for the SC, but the potential benefits to clinical radiology vastly outweigh the hurdles we must overcome. For example, CEST experiments are plagued by confounding effects from the macromolecular component and direct water saturation[6]. The broad saturation line shape of the MT pool

contributes significant saturation effects throughout the CEST spectrum. Rather than eliminate the MT effect as a confound, potentially losing valuable information as well, we use the indices we derive from qMT to 'inform' our CEST quantification technique.

The primary goal of this thesis is to develop and evaluate protein- and myelin-sensitive MRI in the SC of patients with MS, with the intention of identifying biomarkers sensitive to the earliest pathological changes in affected tissue. The techniques developed herein will provide a quantitative and biochemically sensitive toolbox for the SC which can easily be expanded to applications throughout the body. This study offers unique insight into the relationship between sub-voxel, molecular tissue changes and neurological deficiencies, and may potentially inform therapeutic intervention and disease prognosis in the future.

INNOVATION

Aim 1: Develop improved modelling and fitting techniques for assessing Chemical Exchange Saturation Transfer indices.

Goal: The goal of this aim is to develop a quantification method capable of removing or reducing the confounding contributors observed in the CEST spectrum.

Hypothesis: Improved quantification of CEST spectra and providing output indices using Z spectral fitting and exchange-based models, we will deconvolve overlapping signals and improve sensitivity to amide proton signals.

Background

Saturation Transfer

Saturation transfer (ST) is a generic term that describes the transfer of magnetization from molecular solute protons to free water protons. A ST experiment sensitizes the observation to the exchange of magnetization that occurs when the magnetic dipole of a solute proton interacts with water protons in their environment, either through chemical bonds or dipolar coupling[8]. In an ST experiment, the exchangeable proton pool is saturated by a radiofrequency (RF) pulse, applied at the specific (or broad) resonance frequency of the protons of interest. As the solute pool is saturated, transfer of the saturation occurs, and the water pool signal is attenuated. The initial loss of signal, however, is not of a detectable magnitude. The main strength of ST is the fact that the unsaturated water protons, now part of the solute pool, will be re-saturated by the off-resonance RF pulse, and will exchange once again. This process repeats itself until a small concentration of solute molecules creates an appreciable decrease in the bulk water signal[9]. Two main types of ST methods exist in the literature for neuroimaging: Magnetization transfer and chemical exchange saturation transfer.

Magnetization Transfer

Magnetization transfer (MT) is a form of ST experiment in which the solute of interest is the proton group associated with solid-like macromolecules, and in the nervous system are typically thought to be associated with myelin. The protons associated with macromolecules (so-called macromolecular protons), have a T2 relaxation time on the microsecond scale, and,

thus, any transverse signal generated from conventional MRI will de-phase prior to readout[10] thus causing these protons to be invisible to T1 and T2-weighted MRI. However, the slow-tumbling of these macromolecules leads to large dipole-dipole interactions and a spectrally broad absorption line-shape, which we can exploit using ST to generate contrast. Due to the large semi-solid proton pool in myelin, MT has been used as a surrogate marker for myelin density throughout the nervous system[11,12].

The clinically relevant and most basic method for characterizing the observed MT effect is the MT ratio (MTR)[10]. The MTR is defined as:

$$MTR = \frac{S_0 - S_{MT}}{S_0} \qquad \textit{Eq. 3}$$

Where S_0 is the observed MRI signal without performing a saturation pulse and S_{MT} is the observed signal after the MT pulse has been applied. While the MTR has been shown to correlate with myelin[12], it is also dependent on scan parameters, static field strength, field inhomogeneities, and tissue relaxation times[13–15]. The sensitivity to non-physiological values has led to the development of quantitative MT, whereby a model is proposed, and parameters fit from multiple MT-weighted signals. In particular is the development of a two pool quantitative model for quantitative MT experiments[16] which allows for the extraction of indices independent of field strength, relaxation times, and non-physiological parameters. The model uses a two-pool system (**Figure 2**) dictated by the Bloch-McConnell equations, where one magnetization pool is of the macromolecular component (M) and the other from the free water component (F). The model is represented by the following equations:

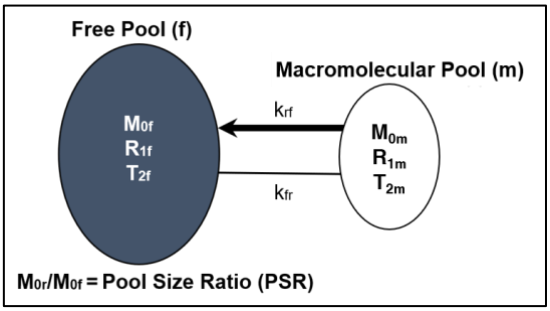

Figure 2. *The 2-pool exchange model using the Bloch equations to describe the transfer of magnetization between the free water and macromolecular pools.*

$$\frac{dM_x^F}{dt} = -\frac{M_x^F}{T_2^F} - 2\pi\Delta\omega M_y^F \qquad \textit{Eq. 4}$$

$$\frac{dM_y^F}{dt} = 2\pi\Delta\omega M_x^F - \frac{M_y^F}{T_2^F} - \gamma B_1(t) M_z^F \qquad \textit{Eq. 5}$$

$$\frac{dM_z^F}{dt} = \gamma B_1(t) M_y^F - (R_1^F + k_{FM}) M_z^F + k_{MF} M_z^M + R_1^F M_0^F \qquad \textit{Eq. 6}$$

$$\frac{dM_z^M}{dt} = -(R_1^M + k_{MF} + \pi\gamma^2 B_1^2(t) g(\Delta, R_2^M)) M_z^F + k_{FM} M_z^F + R_1^M M_0^M \qquad \textit{Eq. 7}$$

where $M_{x,y,z}^{F,M}$ are the x, y, and z components of the magnetization in the free (F) and MT (M) pools. $M_0^{F,M}$ is the equilibrium magnetization of each pool; $\Delta\omega$ and $B_1(t)$ are the frequency offset and amplitude of the saturation RF pulse, respectively; $R_{1,2}^{F,M}$ is the longitudinal and transverse relaxation constant of the two pools; γ is the gyromagnetic ratio; k_{FM} and k_{MF} are the exchange rates from the free pool to the MT pool and vice versa; $g(\Delta, R_2^M)$ is the absorption line-shape of the semisolid pool, a function of bound pool-transverse relaxation and offset frequency. The line-shape can be represented by several different shapes, though super-Lorentzian is considered the most accurate for MT representation *in vivo*[17].

By acquiring MT-weighted data at multiple offset frequencies, we can generate an MT Z spectrum for each voxel[18] (**Figure 3**). To increase the robustness of the fits, often two or more RF saturation powers (given in terms of flip-angle of saturation pulse) are often acquired generating multiple MT Z spectra. The Z spectrum is a term coined by Dr. Bryant to describe and visualize the signal response (i.e. saturation transfer effect) under MT-weighting as a function of offset frequency, which is subsequently normalized to a signal acquisition without MT saturation. The water proton resonance frequency occurs at 0 ppm (on-resonance), and a reduction in the normalized signal can be observed over the offset frequency ranges corresponding to the resonance of the solute proton pool. In a quantitative MT experiment, offsets frequencies are chosen to sample a wide range of signal responses (often offset frequencies are sampled semi-logarithmically) from 1-100 kHz (at 3T, 128Hz ~ 1ppm) to describe the broad, featureless absorption line-shape of the macromolecular pool. The normalized signal is then input into the model, which can estimate

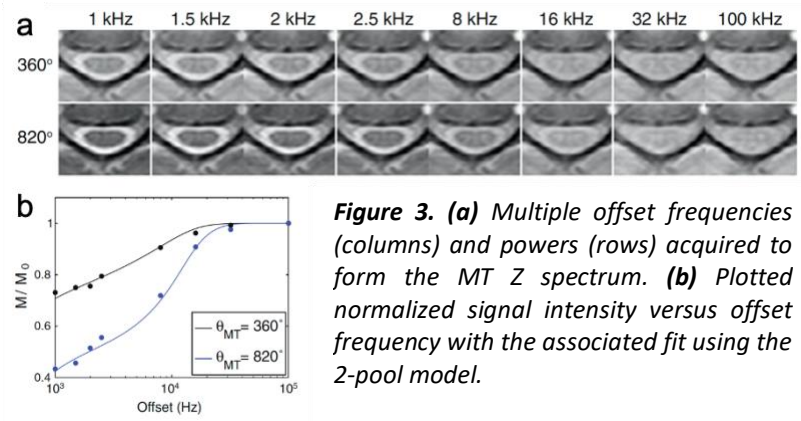

Figure 3. (a) *Multiple offset frequencies (columns) and powers (rows) acquired to form the MT Z spectrum.* ***(b)*** *Plotted normalized signal intensity versus offset frequency with the associated fit using the 2-pool model.*

quantitative indices which, to a first degree, reflect physiological tissue properties. These indices include the pool size ratio (PSR), or the ratio of the macromolecular pool to the free water pool ($\frac{M_0^M}{M_0^F}$); the forward and backward exchange rates between macromolecular and surrounding water protons ($k_{FM,MF}$), and the transverse and longitudinal relaxation times for each pool. The PSR is the most often reported metric, as it has shown a strong correlation to myelin density throughout the CNS[3,4,19,20].

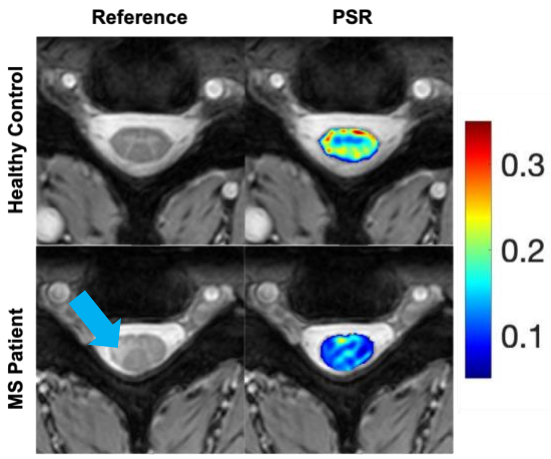

Figure 4. *Anatomical reference and PSR maps for a representative healthy control and an MS patient presenting a lesion (blue arrow). PSR values are reduced throughout the patient's cord when compared to the healthy control, not just at the lesion location.*

Our lab has successfully employed qMT in the SC of MS patients[3,4]. Our results were consistent with previously published qMT studies in the brain[19,20]. qMT is sensitive to MS pathology in the SC, as we found that PSR was higher in healthy WM than in gray matter (GM) or demyelinated MS lesions (**Figure 4**). We expect that the PSR may prove to be an effective biomarker for changes in myelin content throughout the CNS and could potentially play a significant role in the treatment monitoring, and diagnosis of any WM pathologies.

Chemical Exchange Saturation Transfer

Chemical exchange saturation transfer (CEST) imaging is a ST imaging technique that relies on indirectly observing the direct chemical exchange of labile protons associated with smaller, more mobile molecules, compared to MT which focuses on larger, rotationally immobile macromolecules. CEST resembles qMT in that they both utilize the transfer of magnetization from endogenous substances to the bulk water to indirectly detect a biomolecule. However, where qMT uses high power, broad-band saturation pulses applied over a wide range (100s of kHz) of offset frequencies, CEST uses a narrower saturation bandwidth with reduced power applied nearer (±5ppm) the water resonance frequency. This is due to the fact that labile protons associated with mobile molecules resonate at only a few ppm away from the water

resonance. The result is a more spectrally selective and biochemically sensitive method, capable of detecting low concentration (μM to mM range), mobile, endogenous molecules[21].

Viable agents for CEST experiments must contain a proton in its structure capable of exchanging with water (so-called labile proton pool). For CEST, the protons of interest often have exchange rates in the slow to moderate range on the NMR time scale as well as a chemical shift spectrally different from that of water[22]. If we assume a two-pool model with no back exchange (water to exchangeable proton pool), we can create a simplified expression of the proton transfer ratio (PTR)[9]:

$$PTR = x_s \cdot \alpha \cdot k_{sw} \cdot T_{1w}(1 - e^{-t_{sat}/T1w}), \qquad \textit{Eq. 8}$$

in which

$$x_s = \frac{[exchangeable\ proton\ pool]}{[water\ proton\ pool]} = \frac{k_{ws}}{k_{sw}} \qquad \textit{Eq. 9}$$

or, x_s is the fraction of concentration of solute protons to free water protons, α is the saturation efficiency, k_{sw} is the exchange rate from the solute to water, T_{1w} is the T1 relaxation time of the water, and t_{sat} is the time of the saturation pre-pulse. Based on this equation, the CEST effect increases with the concentration of exchangeable protons, the saturation efficiency, and the exchange rate from solute to water. Water longitudinal relaxation also scales the strength of the CEST effect[23]. The most efficient exchange occurs when the applied saturation field is on the order of exchange rate. At higher fields, the CEST effect is expected to increase because the T1 of water increases with field strength, which allows for prolonged storage of saturation, and the spectral resolution is improved (3.5ppm at 3T ~ 450 Hz, while 3.5ppm at 7T ~ 1000 Hz). Thus, CEST experiments can benefit from increased field strength and greater spectral resolution, though these experiments are often plagued by strong field inhomogeneities. The irradiation pulses used to saturate the agent are usually low power in order to avoid spillover saturation to other molecules. The CEST experiment also bears some resemblance to the outputs of MR spectroscopy (MRS) in its ability to reveal information about the biochemical composition of tissues *in vivo*. However, CEST has improved sensitivity to labile protons due to the exchange rate being in the range of 30-1000 Hz, allowing a small molecular pool to detectably attenuate a much larger free water pool.

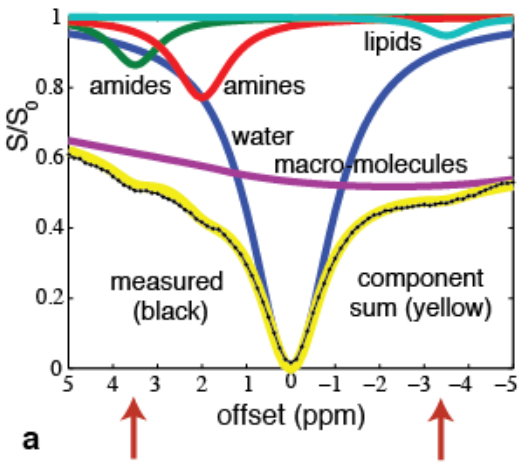

Figure 5. *(Courtesy Dan Gochberg) The measured CEST Z spectrum (black) as well as the various spectral components which contribute to the line shape.*

CEST experiments are also visualized through the use of Z spectra. The CEST Z spectrum, instead of the broad MT spectrum, forms a narrow, asymmetric line shape centered at the resonance frequency of water (0 ppm). Because of the frequency dependence of CEST agents, multiple CEST effects can be visualized with a single Z spectrum as long as the spectral resolution is adequate. **Figure 5** shows the wealth of information contained in just a single CEST Z spectrum. Note that macromolecules and direct saturation have a large influence over the shape of the spectrum and some resonance bandwidths of CEST agents overlap. Because of these confounding influences, it is difficult to ascribe a CEST measurement experiment to the effect of a single exchanging proton pool[24].

The most commonly studied endogenous CEST agents include amine (NH_2), amide (NH), and hydroxyl (OH) functional groups[25]. Different endogenous metabolites have different exchanging groups, revealing specific biochemical information on the tissue being imaged and MR pulse sequences can be designed to exploit, more specifically, individual metabolite pools. The CEST method which focuses on the exchange of amide proton magnetization is known as Amide Proton Transfer (APT) CEST[26]. The most abundant source of amide protons are the amide protons of the amide bond in the protein/peptide backbone. As such, APT CEST experiments can reveal information on the concentration of proteins and peptides as well as the pH of the tissue[26]. Amide protons resonate near 3.5 ppm downfield from water. This shift is larger than most endogenous CEST agents and allows the APT effect to be more easily delineated from direct water saturation[21].

CEST Quantification

One convenient method for characterizing the CEST effect is by looking at both sides of the CEST z-spectrum for any spectral asymmetry. Frequencies both upfield and downfield from water are acquired in CEST experiments in order to quantify the Z spectrum using MTR

asymmetry (MTR_{asym}) analysis[27]. MTR_{asym} is the most common quantification technique for CEST in the literature but, contrary to conventional MTR, MTR_{asym} compares the normalized signal reduction at a particular offset frequency with the normalized signal reduction on the opposing side of the Z spectrum:

$$MTR_{asym}(\omega) = \frac{S(+\omega)}{S_0} - \frac{S(-\omega)}{S_0} \qquad \textit{Eq. 10}$$

where ω is the offset frequency of interest. Working under the assumption that all contributors are symmetric about the water resonance frequency, this method would ideally calculate the signal reduction only due to the amide pool. However, these contributions are intrinsically asymmetric *in vivo* due to a number of exchangeable proton groups on the positive frequency offsets[25], and MT and Nuclear Overhauser effects (NOE) on the negative offsets[28]. NOE represents saturation transfer effects from aliphatic groups and phospholipids[29]. MTR_{asym}, just like MTR, is also sensitive to scan parameters, field inhomogeneities, and tissue relaxation. Despite the issues with this technique, it remains the most often reported output metric because it is computationally straightforward and requires fewer dynamics.

Another factor MTR_{asym} does not consider is that the RF pulse used to saturate these low-concentration solutes will also saturate other nearby resonances. This is especially troublesome for the endogenous CEST pools which resonate close the water peak, where the 'spillover' of direct water saturation reduces sensitivity to the CEST effect of interest[23]. One other major confounder to any CEST experiment is the broad MT effect, which influences the saturation throughout the entire CEST spectrum[26,28]. The issue is amplified in tissues with myelin pathologies such as MS, where changes to the macromolecular concentration may significantly alter the baseline of our CEST spectrum. Higher RF power has been shown to increase both spillover and MT effects[30], yet the observed CEST effect also increases[31]. Therefore, in order to maximize our sensitivity to the CEST effect, we need to develop a more sophisticated, quantitative technique for CEST imaging that accounts for the many overlapping contributors composing an *in vivo* Z spectrum.

There have been a number of approaches developed by the CEST community which attempt to address one or all of these issues. There are model-free techniques such as apparent

exchange-dependent relaxation (AREX)[23,32], or model-based techniques such as Lorentzian fitting[9,33], and multi-pool exchange models[28,30].

AREX is a Z spectrum correction approach using the principles of spin-locking MRI experiments[34] to account for MT, spillover, and T1 effects[23]. A flow chart for calculating AREX can be seen in **Figure 6**. First, a B0 correction technique is applied to the raw Z spectrum, which, in our case, is a WASSR correction[35]. This is common practice in a CEST experiment due to the spectral selectivity of the method. Next, we identify the Z_{label} and Z_{ref}. Z_{label} is the signal in the solute frequency range, while Z_{ref} can be determined in a number of ways, including opposite frequency such as in MTR_{asym}, or estimating the signal using Lorentzian fitting. Then, the purely CEST exchange, or MTR_{Rex}, is calculated using the following formula:

$$MTR_{Rex} = \frac{1}{Z_{lab}} - \frac{1}{Z_{ref}} \qquad \textit{Eq. 11}$$

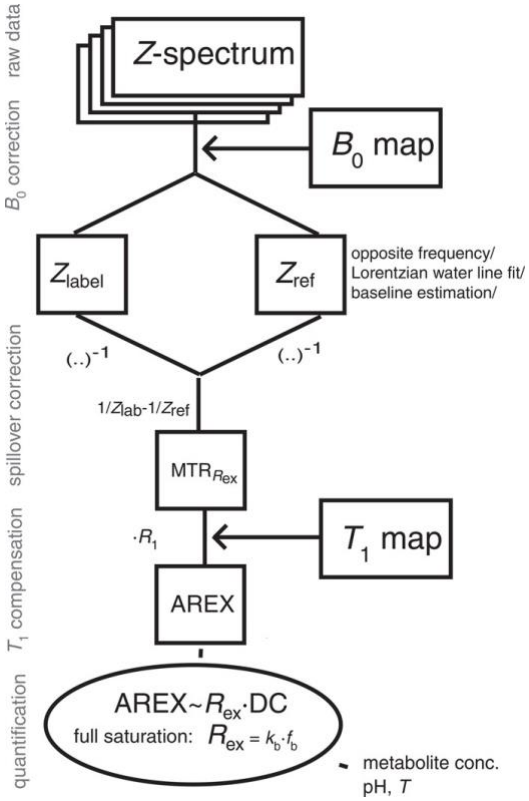

Figure 6. *The order of operation for evaluating spillover- and T1- compensated AREX.*

The opposite frequency method for Z_{ref} also incorrectly assumes that the MT component is symmetric about 0 ppm, so some residual effects from MT will remain. Finally, we apply T1 compensation by multiplying the MTR_{Rex} by a quantitatively derived T1 map, leaving us with a spillover, MT, and T1 corrected AREX metric. Zaiss et al, in the first application of AREX to the brains of human glioblastoma patients, found significant alterations and entirely new features in the CEST contrast of tumors after AREX correction[36], suggesting that previous CEST experiments are heavily biased by DS and MT effects.

Model Based Approaches

Lorentzian fitting, in its simplest form, relies on the knowledge that the direct saturation water resonance can be modeled using a Lorentzian line shape[37]. Thus, any difference from the modeled line shape is assumed to be a result of the CEST effect. This method, known as

Lorentzian difference (LD), addresses DS and removes the need for downfield offset acquisition. However, it still fails to compensate for the asymmetric contributors to the spectrum. Jones et al employed the LD method in the brain and again significant differences were found between LD and conventional MTR_{asym}[33].

More computationally-involved approaches assign each proton pool a Lorentzian with specific amplitude, width, and height parameters, except for the MT pool, which has been found to have a predominately super-Lorentzian line shape[17]. Thus, the labeled Z spectrum saturation (Z_{lab}) can be represented as a baseline saturation (Z_{base}) (which would be 1 with perfect saturation efficiency) minus the Lorentzian components (L_i):

$$Z_{lab} = Z_{base} - \sum_{i=1}^{n} L_i(\Delta\omega) \qquad \textit{Eq. 12}$$

where the Lorentzian line shape is represented by[38]:

$$L_i(\Delta\omega) = 100 - \left(\frac{A_n}{1 + 4\left(\frac{\Delta\omega - \Delta\omega_n}{\sigma_n}\right)^2} \right) \qquad \textit{Eq. 13}$$

where A_n is amplitude, σ_n is the width, and $\Delta\omega_n$ is the chemical shift of the *nth* pool, respectively, and $\Delta\omega$ is the frequency of the off-resonance pulse. **Figure 5** is an example of how the separate Lorentzian line shapes in such a model combine to form a Z spectrum. Lorentzian models show some improvements over MTR_{asym}, in that the calculations no longer require a comparison to the downfield signal, removing influences from downfield contributors such as NOE or MT. However, the model falsely assumes no interactions occur between the pools and has been known to fail with stronger RF pulses where MT and DS effects are more prevalent, or when tissue relaxation times are altered such as in pathology[33]. It has also been shown that CEST pools with smaller chemical shifts may coalesce with the water pool, causing the line shape to no longer resemble a Lorentzian[39]. In short, the Lorentzian approach works well in simulation and phantom data but may lack the complexity to accurately represent the wealth of information contained in an *in vivo* Z spectrum.

The Bloch equations can be used to model CEST data by expanding on the two-pool model shown in **Equations 4-7**[30,40]**.** This representation is an improvement over Lorentzian fitting for *in vivo* data, as it takes into account the underlying physiological parameters of each

labile proton pool, such as concentration, exchange rate, and relaxation time. While this model is capable of extracting a less confounded CEST effect, it is also the most computationally demanding, as well as sequence demanding (more RF saturation powers are necessary to accurately fit the data and avoid overfitting) especially when considering the number of pools which compose a single Z spectrum. An accurate model would need to describe a pool for each CEST agent, DS, MT, and NOE. While this is done frequently in simulation, the amount of data required to fit such a model *in* vivo is overwhelming and not clinically acceptable. Thus, most studies have simplified to a more manageable three-pool model[20,40]:

$$\frac{dM_x^{F,S}}{dt} = -\left(R_1^{F,S} + k_{FS,SF}\right)M_x^{F,S} + 2\pi\Delta\omega M_y^{F,S} + k_{SF,FS}M_x^{S,F} \qquad \textit{Eq. 14}$$

$$\frac{dM_y^{F,S}}{dt} = -\left(R_2^{F,S} + k_{FS,SF}\right)M_y^{F,S} - 2\pi\Delta\omega M_x^{F,S} - \gamma B_1(t)M_z^{F,S} + k_{SF,FS}M_y^{S,F} \qquad \textit{Eq. 15}$$

$$\frac{dM_z^{F}}{dt} = \gamma B_1(t)M_y^{F} - (R_1^{F} + k_{FS} + k_{FM})M_z^{F} + k_{SF}M_z^{S} + k_{MF}M_z^{M} + R_1^{F} \qquad \textit{Eq. 16}$$

$$\frac{dM_z^{S}}{dt} = \gamma B_1(t)M_y^{S} - (R_1^{S} + k_{SF})M_z^{S} + k_{FS}M_z^{F} + R_1^{S}M_0^{S} \qquad \textit{Eq. 17}$$

$$\frac{dM_z^{M}}{dt} = -(R_1^{M} + k_{MF} + \pi\gamma^2 B_1^2(t)g(\Delta, R_2^{M}))M_z^{M} + k_{FM}M_z^{F} + R_1^{M}M_0^{M} \qquad \textit{Eq. 18}$$

where $M_{x,y,z}^{F,M,S}$ are the x, y, and z components of the magnetization in the free (F), MT (M), and solute (S) pools.

While this model is a powerful tool for *in vivo* CEST, it has problems that must be addressed as well. Relayed NOE effects cannot be described by this approach, and are usually ignored or included as a fourth pool[24]. Multiple CEST peaks centered near one another might be interpreted as a single pool. Additionally, even with the three-pool model, acquiring enough data to reliably fit each parameter poses a significant barrier to clinical or routine patient adoption. This is especially true for the MT component, which, in qMT experiments, is fit by sampling over a range of frequencies in the 100s of kilohertz, versus CEST experiments which only cover ±1 kilohertz on average. Other studies have attempted to overcome this by acquiring offsets in the MT range of frequencies during CEST acquisition to better sample the MT line shape[41]. However, this will increase scan time without gaining any additional information on our proton pool of interest.

Methods

In this aim, we will assess the robustness and reliability of the previously mentioned model-based and model-free CEST quantification methods in the presence of MT-altering pathology, while also creating our own informed-CEST approach. That is, can we use the MT effect to better characterize CEST rather than ignoring or devising alternatives to remove it.

Image Acquisition and Processing Protocol

All imaging was done using a 3.0-T, Philips Achieva scanner (Philips Healthcare, Best, The Netherlands). A quadrature body coil was used for excitation and a 16-channel neurovascular coil for reception. All data analyses were performed in Matlab (Mathworks, Natick, MA). The field-of-view (FOV) is centered between the C3 and C4 vertebrae, covering from C2 to C5 over 11 slices. We first acquire a multi-echo fast-field echo (mFFE) as our anatomical reference for registration and segmentation. Parameters include: resolution: 0.65 x 0.65 x 5 mm^3, TR/TE1/ΔTE = 700/7.2/8.8 ms, flip angle (FA) = 28°.

The qMT protocol uses a 3D MT prepared spoiled gradient echo sequence[16]. The MT pre-pulse is a 20-ms single-lobed sinc-Gauss pulse, applied at 2 powers ($B1_{MT}$ = 360°, 820°) and 8 semi-logarithmically sampled offset frequencies (Δω = 1, 1.5, 2, 2.5, 8, 16, 32, 100 kHz). Other parameters include: resolution = 1 x 1 x 5 mm^3, FOV = 160 x 160 mm^2, 2 signal averages, SENSE = 2 (right/left), TR/TE = 50/2.3 ms, FA = 6°. T1, B0, and B1 data were also acquired in the same FOV as the MT data, but with a 2mm resolution. Total scan time for all required qMT sequences was 16 minutes and 45 seconds. The qMT data was used to generate parameter maps using a nonlinear least-squares curve fitting to the 2-pool exchange model described previously. B0 and B1 maps were used to correct offset frequency and RF amplitudes for each voxel, respectively.

The CEST protocol uses a 2D gradient echo with a multi-shot EPI readout (EPI factor = 7). Only a single 20 mm slice was obtained, centered between the C3 and C4 vertebrae. The saturation pulse uses a single 150-ms Gaussian pre-pulse at 2 μT applied at 36 asymmetric offsets sampled between ±5 ppm. The sampling density increases near the APT resonance frequency (between 2 and 4 ppm). Nonsaturated scans were included after every third dynamic (S_0) and respiratory data was collected using a respiratory bellows placed on the subject's

abdomen in order to regress out any respiration-induced signal fluctuation, according to By et al[2]. Additional parameters include: resolution = 1 x 1 x 20 mm^3, FOV = 160 x 160 mm^2, 5 signal averages, SENSE = 2 (right/left), TR/TE = 305/12 ms, FA = 20°. A water saturation shift referencing (WASSR) scan was acquired with each subject for static B0 correction[35]. The total scan time for the CEST sequences was 15 minutes and 10 seconds. For each data set, all qMT and CEST scans were co-registered to the mFFE and GM/WM segmentation was done using Spinal Cord Toolbox (NeuroPoly, Montreal, Canada)[42].

The APT CEST effect was initially calculated using a form of integrated asymmetry analysis in which the area under the curve from both the positive and negative side are used:

$$APT_{asym} = \frac{\int_{-3ppm}^{-4ppm} 1 - S(\Delta\omega)d\omega - \int_{3.2ppm}^{3.8ppm} 1 - S(\Delta\omega)d\omega}{S_0} \qquad \textit{Eq. 19}$$

such that APT_{asym} is expressed in units of percent. A wider range of frequencies is used on the negative side due to sparser sampling; however, it has been shown that the slow-varying NOE signals present in these frequency ranges should not significantly influence our calculations[43].

Results

AREX in the Spinal Cord

The relationship observed between qMT and CEST in this initial analysis revealed that our APT_{asym} metric is heavily biased by competing effects such as DS and the macromolecular component. This is especially true when considering a pathology that changes the macromolecular concentration such as MS. Thus, we sought out alternative quantification techniques which attempt to remove or reduce the dependence of CEST on competing z-spectral contributors, the first of which was AREX.

To date, we have successfully implemented AREX correction to our CEST analysis pipeline. Using the AREX flow chart as a reference (**Figure 6**), we first apply our B0 correction, which, in our case, is done using the WASSR scan. Next, for our Z_{label} and Z_{ref}, we chose to integrate over the same range of frequencies as our APT_{asym} calculation on both sides of the Z spectrum to avoid any bias when making comparisons. Zaiss et al[23], when introducing AREX correction, expressed that defining Z_{ref} in AREX correction is crucial, and that any asymmetry

calculation falsely assumes that the MT line shape is symmetric. Thus, for the *in vivo* analysis, they use a three-point difference technique proposed by Jin et al[44] to avoid contamination from MT, where

$$Z_{ref} = \frac{Z(3\ ppm) + Z(4.2\ ppm)}{2} \qquad \textit{Eq. 20}$$

In all AREX results presented here, we maintained our asymmetry calculation for the sake of comparison. Finally, T1 correction was done using the T1 maps calculated from our MFA sequence, adjusted to match the CEST FOV.

We tested our AREX correction technique on 14 healthy volunteers after informed consent. Representative images from a subject at the C3/C4 level of the cervical SC are displayed in **Figure 7**. Three techniques are compared. First, we used the classic MTR asymmetry method by taking the difference in normalized signal at 3.5 and -3.5 ppm. Also displayed are APT_{asym} and AREX maps. The Z spectrum and AREX-corrected Z spectrum for the same subject can be seen in **Figure 8**. In order to test the effects of AREX correction on changes to tissue relaxation rate and the macromolecular component, we compared WM and GM values in healthy controls. In the figure, the uncorrected spectra have a very similar shape, with two distinctive peaks near our APT resonance frequency.

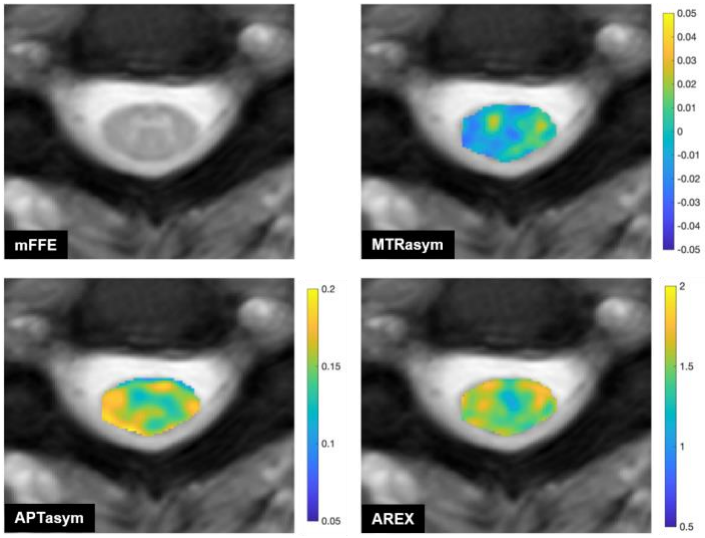

Figure 7. *Anatomical mFFE (top left) and comparison of CEST quantification techniques for representative healthy control*

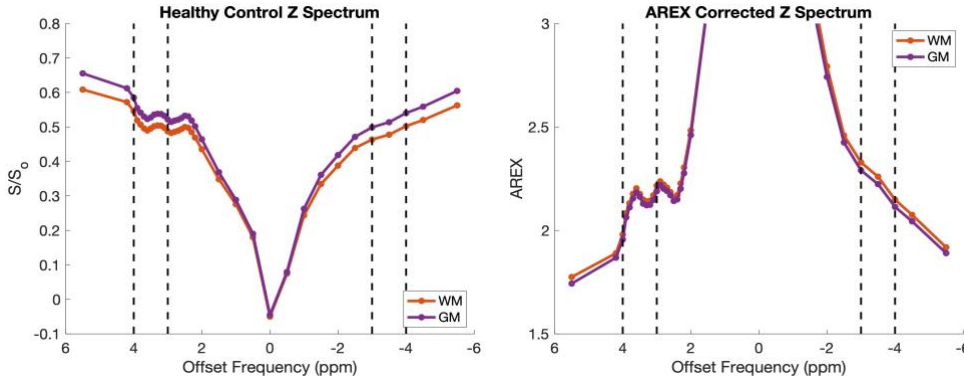

Figure 8. *Z spectra of WM (red) and GM (purple) for representative healthy control subject before (left) and after AREX correction (right) for the same representative healthy control subject.*

However, there is a baseline shift and a narrowing of the water peak in the GM spectra that introduces discrepancies between our line shapes. After applying AREX correction, these discrepancies are significantly reduced, with a near exact match in our APT frequency range, and a much-reduced (but still present) separation on the negative side where MT-contributions dominate. This indicates that AREX does limit the confounding effects of water relaxation and the macromolecular component, though not entirely removing them.

In a full-group analysis we find similar results. **Figure 9** shows a histogram of APT_{asym} and AREX values over all WM and GM voxels for controls.

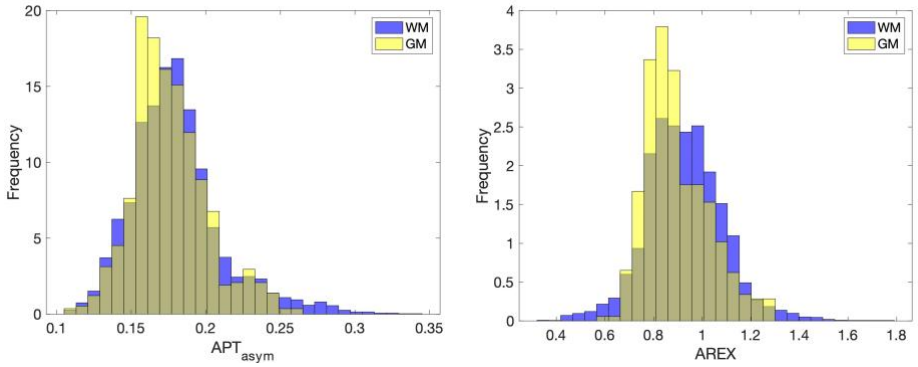

Figure 9. *Histograms comparing APT_{asym} (left) and AREX (right) in GM (yellow) and WM (blue).*

GM values are lower than WM in both indices, though the difference between the two groups was not significant for either method. The separation between tissue types is larger in AREX, as the AREX histogram has an overlap of 33% compared to 52% for APT_{asym}. AREX also follows a more normal distribution in WM (skewness: AREX=0.26, APT_{asym}=1.06).

Lorentzian Modelling

Semi-quantitative methods such as APT_{asym} or AREX, though useful in many applications, will always suffer from certain false assumptions, such as a symmetric MT contribution. Thus, many investigators are moving towards modelling approaches in order to fully separate the individual components which contribute to our signal. MT, as an imaging technique, began with semi-quantitative indices as well, and, as our understanding of the underlying biochemical processes evolved, more advanced modelling approaches were developed which removed many of the dependencies on non-physiological parameters. We hypothesize that CEST will advance in a similar fashion, and, thus, have begun exploring two of the most widely used modelling techniques for CEST: Lorentzian fitting and exchange-based models.

Our work has primarily been in establishing these models for simulation and determining appropriate constraints and bounds for our *in vivo* data. We based our Lorentzian model on Zaiss et al[45]. **Figure 10** shows the results of a 4-pool Lorentzian simulation (APT, MT, DS, and NOE). For each Lorentzian line shape included in the model, there are three parameters which must be solved: amplitude (A_n), is the width(σ_n), and chemical shift ($\Delta\omega_n$). Initial values for simulations were taken from Singh et al[46]. However, these estimates are based on brain data at 7T, therefore we have performed some preliminary testing to determine the accuracy of these estimates in spinal cord data at 3T.

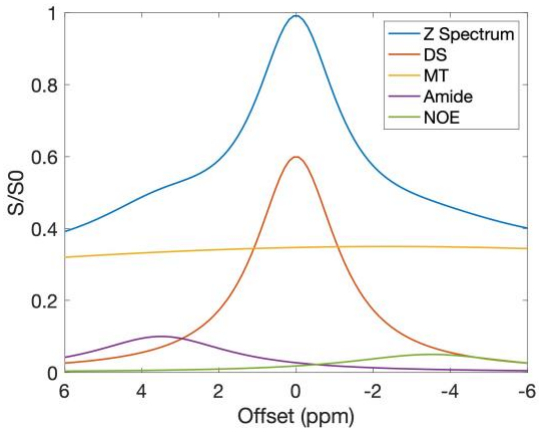

Figure 10. *Four-pool Lorentzian simulation of CEST data. Four pools include: Direct water saturation (red), MT (yellow), amide (purple), and NOE (green). Final Z spectrum (blue) is the sum of each pool.*

Z spectral fitting was performed using the nonlinear fitting 'lsqnonlin' built-in MATLAB function on healthy control data. Estimates and bounds of each parameter in the fitting algorithm can be seen in **Table 1**. We opted to set fixed values for the chemical shift of each species, as these values are more well established by previous research[47,48], reducing the number of parameters to two-per-pool rather than three. Chemical shifts of each species were set as: DS = 0 ppm, MT = -2.4 ppm, Amide = 3.5 ppm, NOE = -3.5 ppm. **Table 2** reports the resulting mean and standard deviation of the amplitude and width estimates for each pool from our fitting algorithm in 14 healthy control subjects. When comparing these results to our initial estimates, we found that amide and NOE pools had a much lower amplitude than predicted and standard deviation often extended past our predetermined bounds. Additionally, in

Table 1. *Initial estimates and bounds for Lorentzian fit of CEST data*

	Amplitudes (%)				Width (ppm)			
	DS	MT	Amide	NOE	DS	MT	Amide	NOE
Lower Bound	20	0	0	0	0.1	10	0.5	0.5
Upper Bound	100	70	20	10	5	100	8	10
Initial Guess	60	35	10	5	2.55	55	4.25	5.25

Table 2. *Results of Lorentzian Z spectral fitting*

	DS	MT	Amide	NOE
Amplitude (%)	60.9 ± 14.8	29.7 ± 7.8	6.00 ± 4.29	2.68 ± 3.20
Width (ppm)	2.35 ± 0.55	57.6 ± 37.0	5.85 ± 3.00	5.16 ± 3.91

each subject at least one parameter hit the upper or lower bounds. The most egregious case is in the width estimates of the MT and amide pools, in which 11 and 12 cases, respectively, reached the upper bounds out of 14 subjects.

Exchange-based Models

Lorentzian fitting, while addressing some of the problems of semi-quantitative approaches, also suffers from false assumptions that will bias our results. As stated previously, Lorentzian models incorrectly assume no interaction between pools occurs and that each pool maintains the predetermined line-shape it is designated[17,23]. Therefore, we have implemented a three-pool exchange model (DS (*F*), MT (*M*), Amide (*S*)). A major issue in modelling CEST using the Bloch equations is the large number of pools which contribute to the final CEST Z spectrum. Some models include upwards of 7 pools to represent CEST *in vivo*, and, while we have implemented our model such that the addition of more pools is possible, we assume that the contributions from other pools will be miniscule. Even with a three-pool model, there are twelve independent tissue parameters which must be solved. Referring to **Equations 13-17**, these parameters include: $R_1^{F,M,S}$, $R_2^{F,M,S}$, $\Delta_{F,M,S}$, $k_{FS,FM}$, and $PSR^{M,S} = \frac{M_0^{M,S}}{M_0^F}$. It has been shown through qMT models that the dependence on $R_1^{M,S}$ is low[14], therefore these values were set to 1 ms^{-1} for fitting purposes. R_1^F is estimated by using MFA data to reconstruct $R_{1,obs}$ maps[40]. The chemical shift of MT, Δ_M, is well-established by literature and can be set to -2.41 ppm[47]. Under normal circumstances, the remaining eight parameters would need to be fit or estimated by some other means. However, by incorporating the results from our qMT experiments, we have voxel-by-voxel values for PSR^M, k_{FM}, and $R_2^{F,M}$, reducing the total number of unknown parameters to four: PSR^S, k_{FS}, Δ_S, and R_2^S. We hypothesize that by including qMT results in our CEST fitting algorithm, we can significantly improve our overall fit and reduce dependence on the MT and DS component.

To date, we have successfully implemented a three-pool model for simulation but have not yet applied the fitting algorithm to heathy control subjects. We have, however, compared our *in vivo* data to simulations using parameter estimates for brain WM from van Zijl et al[9] and mean values of for PSR^M, k_{FM}, and $R_2^{F,M}$ within the WM from the same subject's qMT results (**Figure 11**). The agreement between the two spectra, even without any fitting applied, is

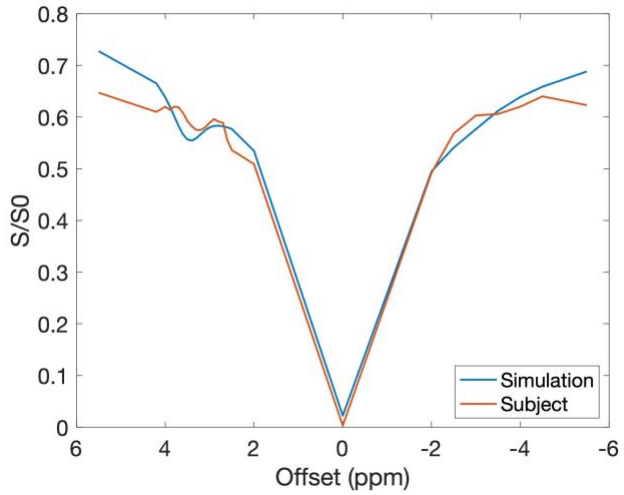

Figure 11. *Healthy control Z-spectrum for WM (red) and 3-pool exchange model simulation (blue) using the same subject's average qMT results and estimated brain WM values for unknown parameters.*

encouraging. As this technique is further developed and explored, we are confident it will prove to be the most effective method in extracting a pure CEST effect.

Discussion

In Aim 1, we have implemented the AREX Z spectral correction approach, and explored two more advanced quantitative methods: Lorentzian fitting and exchange-based models. Our results demonstrate the inherent bias in the most commonly reported CEST quantification technique, MTR_{asym}, and how each of the alternative techniques address these confounders. AREX, a semi-quantitative, Z-spectral correction approach uses inversion and T1 scaling to account for MT, spillover, and T1 scaling effects[23]. Lorentzian fitting is a signal-based model that utilizes the Lorentzian line shape of the individual CEST contributors, assigning each pool a width, amplitude, and chemical shift[38]. The final method presented here, the 3-pool exchange-based model, utilizes the Bloch equations to fit the Z spectrum using the physiological parameters of each labile proton pool[30]. As we progressed through each method, we discussed their inherent false assumptions and how that will influence the contrast of our CEST experiments.

In **Figure 7**, in which we compare CEST measurements in a healthy control subject, the contrast within the cord changes drastically between each of the three methods. The same data analyzed using different methods, despite each one attempting to extract the same information, can produce vastly different results. This illustrates why reproducibility is especially difficult in CEST experiments[24], and also shows the importance of establishing a standard quantitative index for CEST imaging, which may alleviate many of these issues.

Our findings in **Figure 8** demonstrates the reduced influence of the MT component in our AREX-corrected CEST spectrum. By comparing two tissue types which have differing concentrations of the macromolecular component (i.e. gray matter and white matter), we can visualize how the MT contribution shifts the baseline saturation of our uncorrected spectra. It also highlights the importance of addressing the MT pool in CEST experiments, especially those that focus on demyelinating disorders such as MS. Though, as stated previously, AREX will only reduce the influence of MT, and does not remove it entirely. In order to completely separate each individual CEST contributor, more quantitative model-based techniques will be required.

We hypothesize that the T1 compensation in AREX may overcorrect for the CEST effect scaling with water relaxation in some cases, which may be introducing the GM/WM contrast in AREX that we have not observed in APT_{asym}. Conversely, this may be an accurate representation of the APT contribution, as little is known on the relative concentrations of proteins between GM and WM in the SC. Our findings suggest that AREX is an overall improvement over APT_{asym} and reduces the dependence on confounding contributors in CEST experiments.

In general, we find that any CEST contrast computed using asymmetry analysis will be confounded by the macromolecular and NOE pools. However, fitting and model-based approaches can potentially remove this bias and reduce the overall sensitivity to non-biological factors such as field inhomogeneity and saturation parameters.

Some studies focus on removing the MT effect as a confound, yet our qMT experiments show us that there is valuable information relating to pathology within this line shape. An alternative approach to model the MT component in a CEST experiment is to acquire both MT and CEST data, quantify the MT parameters using the qMT model, then input those estimated parameters into our CEST analysis. To the author's knowledge, similar methodology has only been applied in two studies[49,50]. Heo et al used the extrapolated MT component from the qMT model as reference signals in a CEST asymmetry analysis[42]. They found that this method enhanced APT-contrast when compared to conventional MTR_{asym} in a rat glioma model at 4.7T. Mehrabian et al used qMT parameters to inform a Lorentzian model in glioblastoma patients[51]. No studies have directly applied the qMT parameters into a multi-pool CEST model, nor has anyone applied the informed CEST technique to a pathology in which the MT component

undergoes significant change such as MS. We hypothesize that in order for CEST to progress towards clinical translation, it will be essential to address both the mobile (CEST) and semi-mobile (MT) solutes which comprise the *in vivo* Z spectrum.

If one were to continue building upon the foundations of the work presented here, the author recommends identifying alternative methods of defining Z_{ref} in AREX calculations, such as the three-point method and using modelling to perform Lorentzian difference measurements. Choice of reference signal has drastic implications on the final outcome of CEST experiments. For example, by defining Z_{ref} as the opposite frequency signal as we have done here, we introduce confounding effects from MT and NOE, which contribute to the overall signal within these frequencies. Thus, in semi-quantitative AREX calculations, methods which reduce dependence on other contributors to the CEST spectrum, such as the methods listed above.

In order to improve Lorentzian model, recommend using qMT data, primarily the transverse relaxation rates of the MT and water pools, to inform the line shapes. Though, the initial focus should be on identifying the components derived from qMT data that best reduce the degrees of freedom of the fitting of the CEST spectrum in both Lorentzian and exchange-based models. Our model-based approaches were only introduced in this Aim and, in the future, we would like to perform a more thorough analysis. But our initial findings for Lorentzian fitting suggest that the amplitude and width of our various CEST contributors may be significantly different than the values seen in the brain, especially the amide and MT component. Therefore, specific spinal cord-related values will need to be determined for the Lorentzian fit.

Conclusions

Our investigation into advanced quantitative methods for CEST experiments has demonstrated the inherent bias in many of the techniques used in the literature today. MTR_{asym}, the most commonly used CEST quantification technique, is sensitive to scan parameters, field inhomogeneities, tissue relaxation, and influence from the many contributors to the CEST

spectrum. If one intends to extract a measurement based solely on amide concentration within a voxel, then a shift towards more quantitative techniques will be required.

Aim 2: Evaluate the sensitivity of saturation transfer experiments to pathological changes of both ordered (Aim 2a) and disordered (Aim 2b) tissues in patients with Multiple Sclerosis.

Goal: Assess sensitivity of improved qMT and CEST models to study disease presentation and evolution in both the spinal cord and CSF.

Hypothesis: Indices derived from quantitative saturation transfer experiments will provide more specific biochemical information that can be related to the progression and severity of tissue damage in vivo.

Aim 2a: Application to Ordered Tissues

Background

The SC is involved in MS pathology, with up to 90% of MS patients exhibiting lesions in the SC[1]. MS is an autoimmune disorder of the central nervous system (CNS), characterized by demyelination, inflammation, and axonal degeneration[52]. The course of MS is highly variable and difficult to predict. Severity of the disease is gauged using the Expanded Disability Status Scale (EDSS), which provides a numerical value from 1 to 10 depending on how significantly the patient's life is negatively affected by the symptoms of the disorder[53]. Neurodegeneration begins at the earliest stages of disease development, meaning that the most important step to intervention and effective therapeutic treatment is early and accurate diagnosis, which current diagnostic methods are lacking[54].

There are four primary phenotypes of MS: relapsing remitting (RRMS), secondary progressive (SPMS), primary progressive (PPMS), and progressive relapsing (PRMS). For the purposes of this study we will be focusing mainly on RRMS, the most common form of the disease, affecting 85% of all MS patients[55]. RRMS is characterized by clearly identifiable attacks of increasing neurological symptoms followed by periods of remission where symptoms may lessen or fail to progress any further[55].

The primary index for qMT, PSR, provides a surrogate marker for myelin concentration in a voxel[56]. The early stages of MS, prior to demyelination, is characterized by the infiltration of protein-rich inflammatory components due to the autoimmune response[55]. Thus, an imaging marker sensitive to protein concentration such as APT CEST, could highlight these initial pathological tissue changes. We hypothesize that, by utilizing these methods in tandem, we will reveal specific pathological information relating to the earliest stages of disease progression in MS. The goal for this aim is to evaluate not only what our indices can tell us about pathology, but also what pathology can tell us about our indices. In the following aim, we will examine the sensitivity of each derived index to clinical presentation as well as how the quantitative models respond in pathology.

Methods

In a preliminary study to assess repeatability and sensitivity to disease progression, three healthy volunteers (2F/1M, 39±10 years of age) and four mildly-affected relapsing remitting MS patients (2F/2M, 40±8 years of age, low disability) were scanned twice with an average of 1.24 years between scans. All MS patients' disability was rated using the EDSS score by their respective clinicians. At the time of the study, all patients met the McDonald's diagnostic criteria for MS and had concomitant brain lesions confirming MS diagnosis. In addition to our imaging protocol described in Aim 1, we also acquire sensorimotor testing. Prior to MRI, all participants underwent a timed 25-foot walk test and timed up-and-go (TUG) test.

The lateral, dorsal, and ventral WM columns were segmented and analyzed for spatial differences. A nonparametric Wilcoxon rank sum test was performed to evaluate group differences in the mean APT_{asym} and PSR values between healthy WM and both normal appearing WM (NAWM) and lesions for MS patients.

Results

qMT and CEST in WM Pathology

Table 3. *Mean PSR (top) and APT_{asym} (bottom) values within the WM and NAWM of healthy control and MS patients, respectively.*

APTasym (%)	Scan 1	Scan 2
Control	18.1±1.4	18.8±1.3
MS Patients	18.5±3.0	19.3±1.5
PSR (%)	**Scan 1**	**Scan 2**
Control	18.8±1.3	19.0±1.5
MS Patients	17.5±2.7	16.2±2.0

Table 3 contains mean PSR and APT_{asym} values within the WM and NAWM. A repeated measure, non-parametric ANOVA revealed no significant change between scans within groups. We observed a lower PSR in MS patients and slightly higher APT_{asym} when compared to healthy controls, though these differences were not statistically significant (Wilcoxon rank sum test) likely due to the small sample size. Also note that the PSR values in MS patients show a decrease over time that we do not observe in healthy controls.

Despite the lack of statistical significance, clear differences can be observed when comparing the average WM and NAWM Z spectra for both scans (**Figure 12**). Minimal change is observed in the healthy controls between time points, especially within the APT frequency range. However, this is not the case in the MS group, where we see significant variation throughout the spectrum. Importantly, the baseline of the CEST z-spectra in the MS patient appears to be higher on follow-up than for the initial scan. We propose that this is due to a reduction in the MT component (i.e. demyelination) which causes the baseline to appear less saturated throughout the frequency range of interest. This further highlights the importance of characterizing both the MT and CEST effects when considering pathological changes over time.

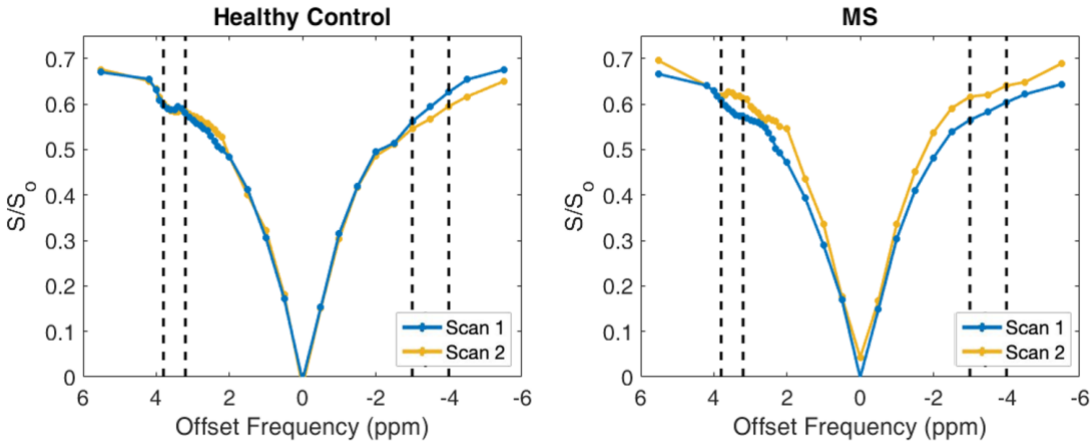

Figure 12. *Average WM Z spectra for healthy control (left) and MS patients (right) at time point 1 (Blue) and time point 2 (Orange). Dashed lines indicate the region of integration for APTasym calculation.*

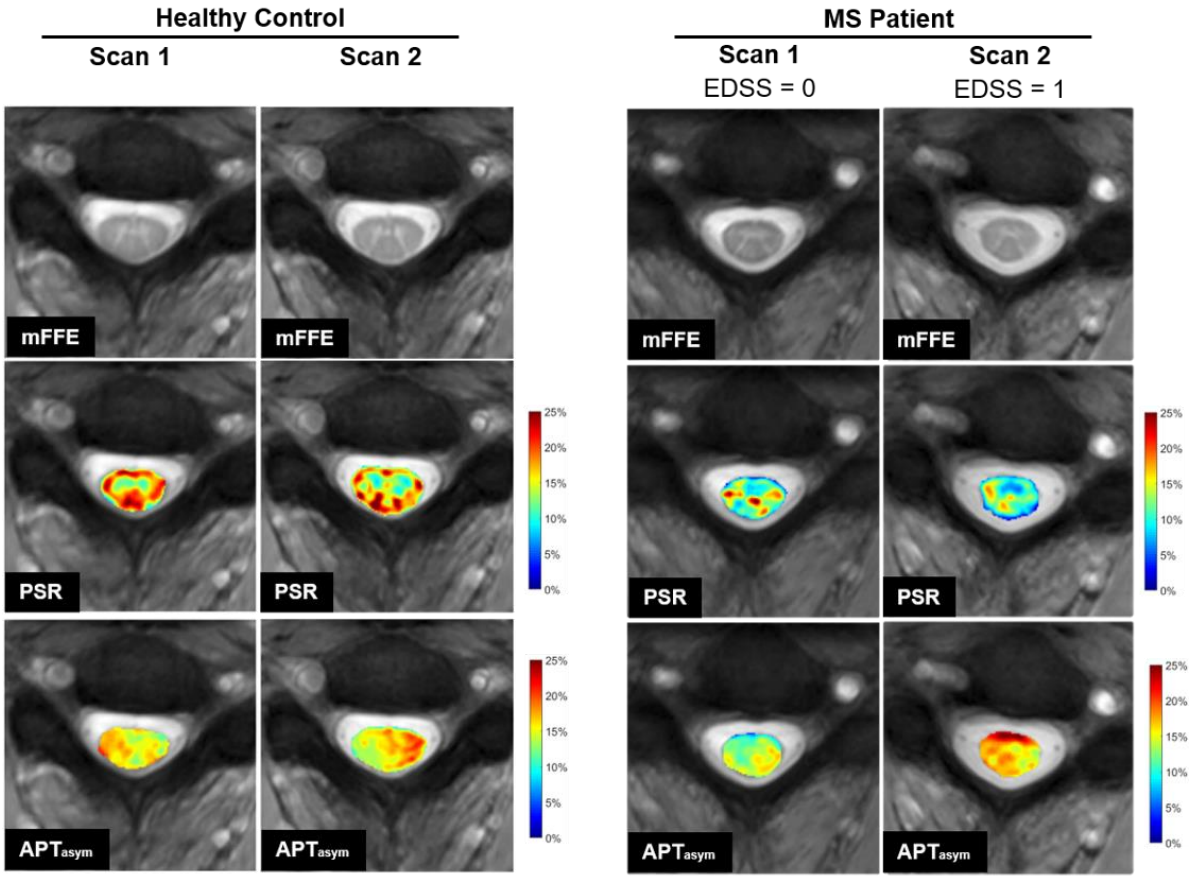

Figure 13. *Longitudinal imaging results for a healthy control (left) versus an MS patient (right). Anatomical images (top row), PSR maps (middle), and APTasym maps (bottom) at each time point are shown.*

Overall, our results highlighted the heterogeneity of MS pathology, and many of the changes we observed were specific to each patient. **Figure 13** presents two individual case studies, one a representative healthy control, the other a low-disability RRMS patient. It is important to note that this MS patient was our only subject whose disability score increased during the time of this study, going from and EDSS score of 0 to 1. In the anatomical scans, there are few visible changes in either subject and no lesions present at either time point in the MS patient. In the PSR maps, the control shows clear contrast between the WM and GM. As expected, we see higher PSR values where macromolecular component is larger (WM), and this contrast is maintained longitudinally. However, this is not the case in our MS subject, where GM/WM

Table 4. *Cross-cohort AREX Demographics*

	MS Patients (n=11)	Controls (n=14)
Sex	8F/3M	9F/5M
Age, mean ± SD	46.4 ± 10.1	39.2 ± 12.3
EDSS, median (range)	2 (0-5.5)	-
Disease Duration, mean ± SD	8.6 ± 3.9 years	-

contrast is almost completely lost, and reduced PSR values are seen throughout the white matter, despite there being no visible lesions in our mFFE. The APT_{asym} maps for our healthy control show some spatial variation, but the mean value within the white matter stays relatively constant (ΔAPT_{asym} = 1.4%). This is not the case in our MS subject, where we see a large increase in values between time points (ΔAPT_{asym} = 5.98%).

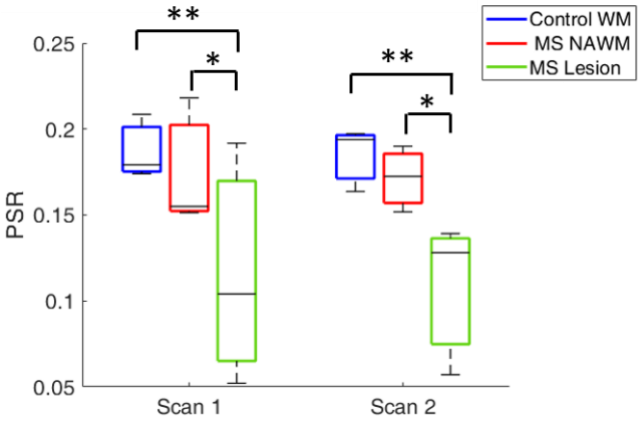

Figure 14. *Box plots of the mean PSR values within three tissue types: healthy control white matter (blue), MS patient normal appearing white matter (red), and lesions (green) at both time points. (*: p = 0.01, **: p < 0.001)*

A triained clinician identified lesions in 3 out of 4 MS patients. However, our reduced CEST FOV did not capture any of these lesions. **Figure 14** contains a box plot of mean PSR values within three tissue types: healthy control WM, NAWM, and MS lesions. Significant differences were found between control WM and lesions (p<0.001), and NAWM and lesions (p=0.01) at both time points. Also, the change in PSR over time was very similar between NAWM and lesions, indicating that lesions do not show an increased rate of demyelination when compared to the surrounding NAWM.

AREX in WM Pathology

After successfully implementing AREX correction on control data in Aim 1, we applied AREX in a cross-cohort analysis of both low and high disability MS patients. Demographics for this study can be seen in **Table 4**. **Figure 15** displays the original Z spectrum compared to the AREX-

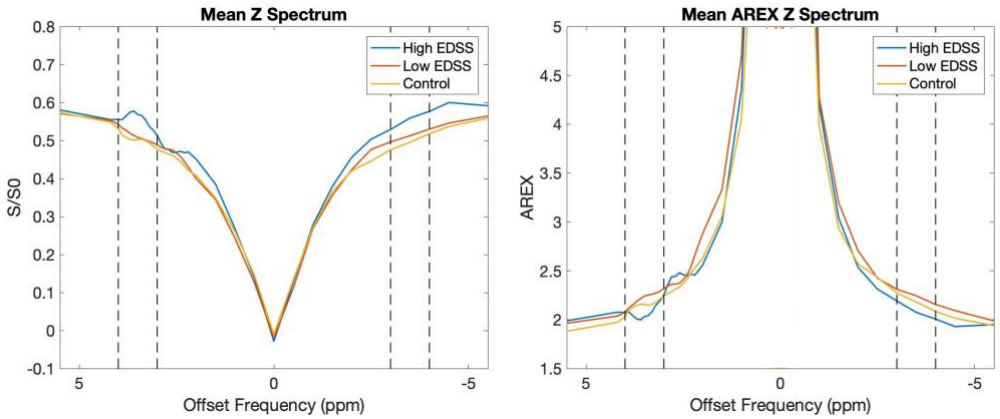

Figure 15. *Mean, uncorrected Z spectra within WM (left) and AREX corrected spectra (right) for three groups based on disability: control (yellow), low disability (red) and high disability (blue).*

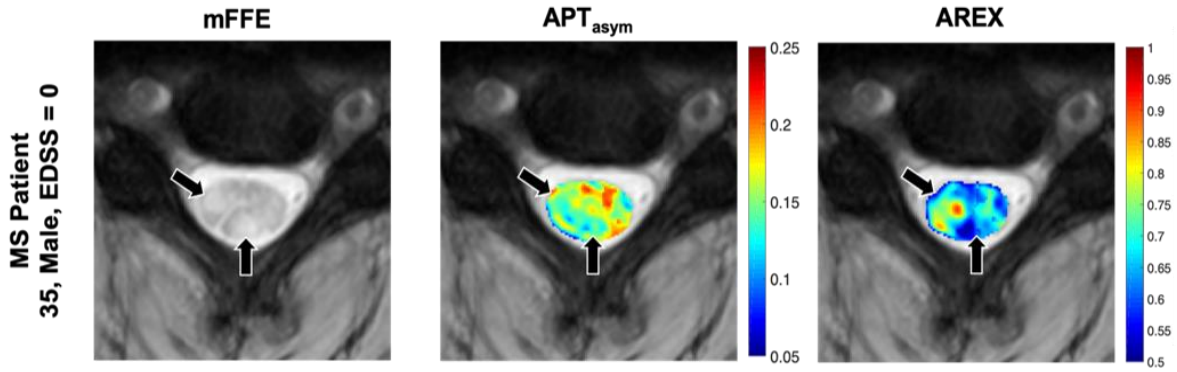

Figure 16. *Representative anatomical (column 1), APT asymmetry (column 2), and AREX (column 3) maps for an MS patient with an EDSS of 0. Lesions were identified in two locations within the CEST FOV, indicated by black arrows.*

corrected spectrum of healthy control, low EDSS, and high EDSS groups. On the AREX-corrected spectrum, we observed an increased delineation between our groups within the APT frequency range and a reduction in the separation on the negative side. A Pearson Correlation Coefficient test revealed that our AREX indices also significantly improve our correlation to important clinical measures and sensorimotor testing (**Table 5**), although correlation to overall disability remains poor. A Wilcoxon rank sum test revealed no significant differences between controls, high EDSS, and low EDSS groups for either AREX or APT_{asym}.

p-value	**AREX**	**APT_{asym}**
MS Duration	**0.037**	0.675
Walk Test	0.213	0.912
TUG	0.198	0.887
EDSS	0.627	0.701

Table 5. *p-values of correlation analysis between CEST indices and clinical measures of disability.*

We also explored grouping by tissue type (healthy WM, NAWM, and lesions) rather than overall disability. **Figure 16** shows an MS patient's mFFE, as well as overlaid APT_{asym} and PSR maps. Two lesions were identified by a trained clinician and manually segmented, one in the dorsal column and one in the right lateral column (indicated by black arrows). The APT_{asym} map shows contrast changes associated with the location of these lesions, while the AREX map does not.

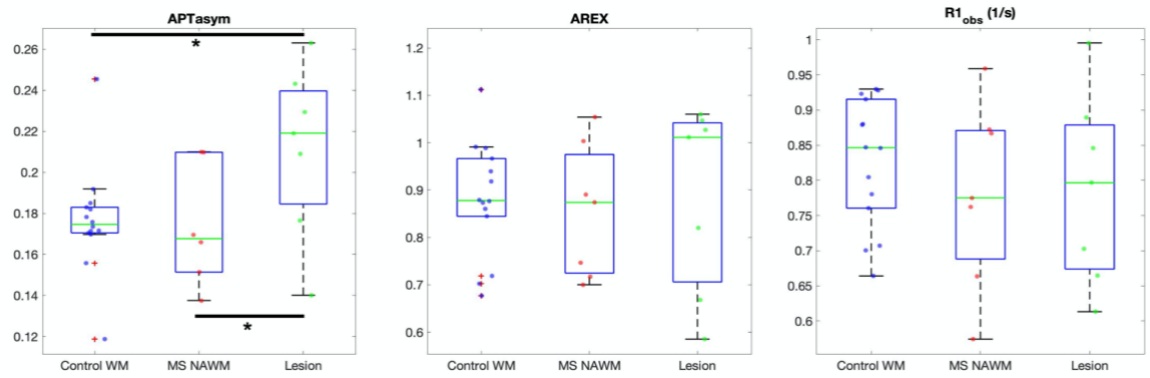

Figure 17. *Mean APT asymmetry (left), AREX (center), and R1 (right) values for each subject, grouped by tissue type: healthy control WM (blue dots), MS NAWM (red dots) and lesions (green dots). (*: p<0.05)*

Figure 17 contains box plots comparing mean values within the WM for APT_{asym}, AREX, and R1 indices. A Wilcoxon rank sum test revealed that APT asymmetry increases significantly in lesions (green dots) when compared to healthy control WM (blue dots) and NAWM (red dots). However, this difference is lost after correcting for MT and T1 effects using AREX. In the R1 plot, we observe a slight decrease in NAWM and lesions, as was expected, but, again, no significant differences. Our results suggest that the sensitivity of uncorrected CEST metrics to lesion tissue is confounded by contributors such as the macromolecular component and changes to longitudinal relaxation.

Discussion

The results of Aim 2a demonstrate that CEST and qMT are able to detect significant alterations in the biochemical composition of spinal cord tissue in MS patients, even those who only exhibit mild disability. We observed PSR and APT_{asym} values in MS patients and healthy controls at two time points, demonstrating how the longitudinal progression of these two indices change in a patient population. We also investigated AREX quantification in a cross-cohort analysis, comparing it to our original CEST metric, APT_{asym}, and found that AREX significantly improves correlations to clinical measures of disability in MS patients. We also found that AREX correction alters CEST contrast, reducing sensitivity to lesions.

Our lab has published individual findings on CEST[2] and qMT[3,4] in the spinal cord, however, to date, no studies to the author's knowledge have examined both qMT and CEST

results in the spinal cord in tandem. Additionally, no studies have applied AREX correction to *in vivo* spinal cord imaging.

Our results show the complex interplay between these two techniques and how they may be used to inform each other and further our understanding of MS pathology. Despite a repeated measured ANOVA failing to reveal significant changes to APT_{asym} and PSR, the decrease over time observed in the PSR of our MS cohort is consistent with the demyelination which occurs in MS. We hypothesize that, even in low disability patients, demyelination is constantly occurring within the cord, leading to a decrease in PSR, though the rate of demyelination may change depending on if the patient is in a relapsing or remitting phase. Additionally, the overall changes in our CEST data are better represented by the mean Z spectra (**Figure 12**). Most notably, the baseline saturation shifts upward between scans. This is representative of a decreased contribution from the macromolecular pool, most likely due to demyelination in our MS group as the disease has progressed. Additionally, if we examine only the frequencies within our APT integration range (3.2 – 3.8 ppm), the control group presents a larger 'dip' in the spectrum which is indicative of a larger CEST effect and, one would assume, larger APT_{asym} values. However, this is not the case, as we see higher APT_{asym} values in the MS patients due to the shift observed in the negative side of the spectrum, again demonstrating the large influence MT has over our CEST indices.

The representative control and MS patient maps in **Figure 13** reveal valuable information concerning the progression of these indices. Despite no apparent differences in the anatomical images, we observe significant alterations in the quantitative maps of the MS patient in both cross-cohort and longitudinal comparisons. Again, we see a decrease in the PSR throughout the spinal cord consistent with the progressive demyelination seen in MS. This decrease is not localized to lesions, suggesting that demyelination occurs throughout the cord prior to lesion formation. The large increase in APT_{asym} values seen in this patient, who also showed an increase in disability between scans, was not observed in patients whose disability remained stable. Because CEST is sensitive to proteins and peptides[21], we hypothesize that this increase may be due to an influx of inflammatory components invading the tissue in conjunction with a relapse in symptom severity.

Our cross-cohort examination of AREX in the spinal cord further emphasizes the necessity of an improved quantification technique. In **Figure 16**, we see that AREX removes contrast changes associated with lesions seen in our APT_{asym} metric. This, along with the box plots seen in **Figure 17**, lead us to suspect that the uniform decrease seen in our APT asymmetry values within lesions is primarily due to the demyelination influencing the macromolecular contribution. Once these contributions are removed and only the CEST component is present, lesions have a similar presentation to the surrounding NAWM. We hypothesize that the AREX metric gives a much more valid estimation of CEST contributions, despite this nonuniformity, and may reflect the activity of the lesion.

This preliminary longitudinal study, while revealing valuable information on tissue pathology, also highlighted some of the weak points of our methods. It became clear that our CEST quantification method was heavily biased by other confounding contributors to our spectrum, which was our primary motivation for Aim 1. Additionally, vital information could have been contained in the lesions that were not captured by our reduced CEST FOV, thus, in the future, we intend to seek methods to reduce scan time enough that multi-slice acquisition is possible. Possible techniques include sensitivity encoding, compressed sensing, and keyhole imaging. Our small sample size and low disability seen in our MS patients also fails to accurately represent the heterogeneity observed in this population. In the future, we also hope to apply the advanced quantification techniques explored in Aim 1 in both cross cohort and longitudinal studies.

<u>Conclusions</u>

The first combined qMT and CEST *in vivo* study has been reported. Our results demonstrate the potential of each technique as biomarkers for the progression of MS, PSR as a marker for demyelination, and APT_{asym} or AREX as a marker for inflammation. We also reveal the influence confounding factors such as MT and water relaxation have on CEST data in a patient population and demonstrate how AREX can be used to reduce or remove these influences. As these methods are further developed, qMT and CEST may prove to be valuable tools in monitoring

disease progression and response to therapy in MS and a number of other neurological disorders.

Aim 2b: Application to CSF

Background

CSF is a clear, serum-like liquid which occupies the space between the arachnoid membrane and pia matter and is responsible for protecting the brain and SC from trauma, supplying them with nutrients, and removing waste products. As such, CSF provides an ideal window into CNS pathology. Analysis of CSF has been a crucial factor in confirming MS diagnosis, as one of the primary indicators stated by the McDonald's Criteria is the presence of oligoclonal bands or elevated IgG levels in the CSF[57], which are indicative of increase intrathecal protein synthesis and neuroinflammation[58].

Appearance of OCBs in the CSF of a patient with clinically isolated syndrome is also indicative of the future development of MS[59]. While elevated IgG is the most commonly reported pathological change in the CSF of MS patients, standard electrophoresis has identified a number of other proteins which show promise as potential biomarkers when expressed in abnormal amounts. Among these are byproducts of the demyelination process, known as "myelin basic protein-like material" (MBPLs), which have been shown to accumulate in the CSF during the acute exacerbations of RRMS patients and may serve as a marker for acute CNS myelin damage[60,61].

Despite its profound capacity as a tool for diagnosis and disease monitoring, there currently exists no non-invasive, *in vivo* method to detect pathological changes in CSF. Currently, the only means of extracting a sample of CSF is through a lumbar puncture (LP) procedure. LPs are not only highly invasive but may also only reflect the composition of CSF at the lumbar region of the spine which may not accurately represent the total systemic changes that occur. If successful, this study will not only provide a robust, novel, quantitative tool to detect the pathological changes and identify neuroinflammation in cervical SC CSF *in vivo*, but may also offer insight into the relationship between CSF composition and the physical and neurological impairment of patients suffering from MS.

In the following Aim, we apply novel quantitative imaging approaches which have not yet been explored in the CSF by building upon methods which our lab has previously developed to acquire robust, high resolution APT CEST in the SC[2–4]. This work intends to develop biomarkers for MS and improve our diagnostic and prognostic capabilities *in vivo*. We assess APT CEST as a tool to detect neuroinflammation and elevated IgG protein levels, potentially removing the need for lumbar puncture, as well as the sensitivity of qMT to increases in MBPL concentration. The techniques we develop can be translated to any clinical MRI scanner and will have implications in all MS subtypes and a number of other inflammatory or demyelinating neurological disorders such as transverse myelitis, SC trauma, Alzheimer's disease, and adrenomyeloneuropathy. While this thesis will address quantitative imaging of CSF in the cervical spine, it will also provide a foundation for application to CSF in the brain and ventricles. Lastly , the pediatric MS population, which is showing increased incidence[62], could greatly benefit from the non-invasiveness of the proposed study.

Methods

A preliminary study has been performed to assess the sensitivity of our CEST metrics to pathological changes in the CSF. Eight healthy volunteers (4M/4F, 23-55 years of age) and eleven MS patients (2M/2F, 30-58 years of age, average EDSS: 4, average disease duration: 11 years) were recruited after signed, informed consent. The CSF was manually extracted using a region of interest drawn around a portion of CSF and the mean APT_{asym} for the CSF was reported. A Wilcoxon rank sum test was performed to determine if CSF APT CEST effect was significantly different between the healthy control and MS cohorts. We chose to use the APTasym measure because the CSF is expected to have a minimal MT component.

Results

Figure 18 compares the Z spectra of CSF versus SC tissue in our healthy control group.

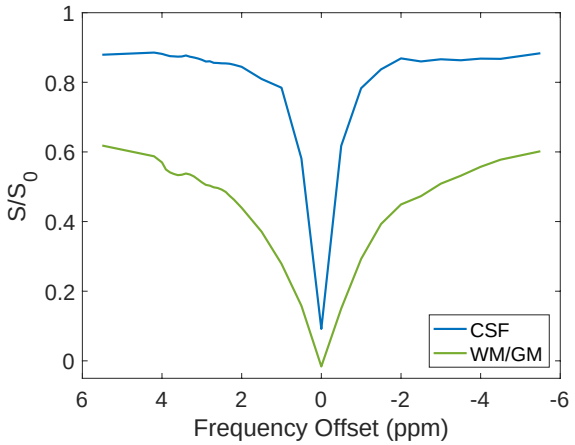

Figure 18. *Comparison of healthy control WM Z spectra in the SC (green) versus CSF (blue).*

The CSF spectra shows two main differences: a narrower peak and an up-shifted baseline. The first can be attributed to the longer relaxation times in liquids versus ordered tissue[13]. The baseline shift seen in **Figure 18** is representative of the lack of a substantial macromolecular pool in CSF. As we have seen through the demyelination in MS, a lower MT pool will shift our baseline saturation upwards. This is another advantage of applying CEST in the CSF, as the influence of the MT component on our spectrum is largely removed.

A Wilcoxon rank sum test was performed on mean APT_{asym} values within the CSF between the healthy control and MS cohorts. Significant APT_{asym} increases in our MS group were noted ($p<0.001$). The mean z-spectra for both healthy and MS subjects are shown in **Figure 19**, as well as the 95% confidence interval (CI) for the healthy controls. The MS Z spectrum lies outside the CI of controls throughout the entire frequency range. Of note, we also see a dip in the signal of the MS spectrum within the APT range that is not seen in controls, which is further corroborated by mean APT_{asym} values (Control: 0.508±0.23%, MS: 0.809±0.39%).

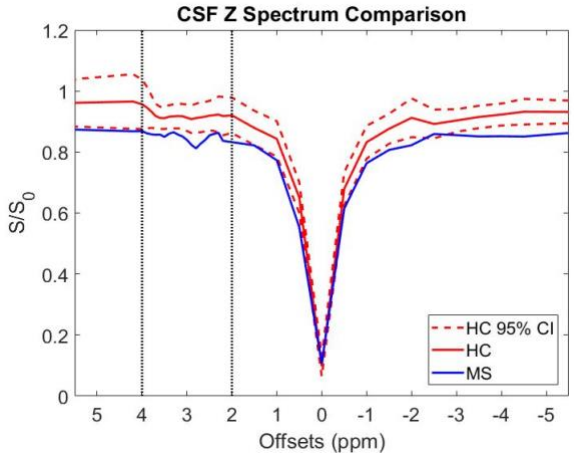

Figure 19. *Mean Z spectrum for control (red) and MS (blue). Dashed lines indicate the 95% confidence interval for the control group. Vertical dashed lines indicate region of APT CEST effect.*

<u>Discussion</u>

In this final aim, we demonstrated CEST as a tool for evaluating the biochemical composition of CSF in MS patients, which may prove to be an invaluable resource in diagnosis and disease monitoring. We compared the CEST Z spectra in ordered tissues such as WM to disordered tissue (CSF), and performed a cross-cohort comparison, revealing significant changes in the CEST spectra of MS patients when compared to healthy controls.

Conventional MRI of the CSF has been limited to flow dynamics and volumetric measurements for a number of reasons. For one, there is little to be gained from standard T1- and T2-weighted images of the CSF, and, until recently, no MRI methodology existed which

could provide sub-voxel, biochemical information on the tissue in question. Also, CSF MR images are typically fraught with artifacts due to turbulent fluid motion[63]. Thus, this is the first study exploring the possibility of applying quantitative MRI sequences other than flow dynamics to the CSF.

In the comparison of the mean Z spectrum in the spinal cord to the CSF (**Figure 18**), there are two important variations: the narrowed water resonance peak and the upward shift in the baseline saturation. As stated previously, the narrow peak can be primarily attributed to the longer T1 observed in CSF. The long T1 of CSF will not only narrow the water peak, thereby reducing DS spillover, but will also allow for more CEST exchange to take place, as the CEST effect scales with T1[22]. Both of these changes should significantly increase the prevalence of any APT contributions to our spectrum, counteracting the lower concentration of CEST constituents in the CSF. The baseline shift, attributed to the lack of an MT component in the CSF, will also improve the sensitivity of CEST to changes in protein and peptide concentrations in the CSF, as the confounding MT factor present in most CEST experiments is significantly reduced.

Our statistical analysis revealed a significant increase in APT_{asym} values in the CSF of MS patients when compared to healthy controls. This difference is clearly displayed in the mean Z spectra of our two groups in **Figure 19**. We hypothesize that the downward shift observed in the MS group spectrum is due to the accumulation of demyelination byproducts such as MBPLs increasing the MT contribution to the signal[64]. To further investigate this hypothesis, the author suggests a cross-cohort qMT experiment in CSF. While the variance of the mean spectra presented here is large, a trend towards increased CEST effect in the MS patients is noted.

If one were to continue investigating CEST in the CSF, the first step should be to acquire CSF samples from clinical lumber puncture for ex vivo testing. Analyzing CEST data *in vivo* versus *ex vivo* could provide a greater understanding of the contrast method as it relates to CSF and the underlying physiological changes. It will also reveal the influence that flow artifacts have on *in vivo* data.

The CSF CEST data should be compared to clinical evaluations of CSF, such as a Western blot test, to verify the presence of immunoglobulins[58]. A notable issue with using a Western

blot to corroborate findings is its inability to detect protein concentration. Western blot is capable of revealing the presence of certain proteins, however, it provides no information on the amount of said proteins in the CSF[65]. For more information on protein concentration, a full spectroscopy may be required.

Conclusions

Here we present the initial findings of the first study to investigate the biochemical composition of CSF using APT CEST MRI. While this study had a small population, it demonstrates that CEST is capable of detecting pathological changes to the APT effect in the CSF, and that changes to the macromolecular component may also be present.

REFERENCES

1. Bot JCJ, Barkhof F, Polman CH, et al. Spinal cord abnormalities in recently diagnosed MS patients: Added value of spinal MRI examination. *Neurology*. 2004;62(2):226-233. doi:10.1212/WNL.62.2.226
2. By S, Barry RL, Smith AK, et al. Amide proton transfer CEST of the cervical spinal cord in multiple sclerosis patients at 3T. *Magn Reson Med*. 2017;79(2):806-814. doi:10.1002/mrm.26736
3. Smith AK, Dortch RD, Dethrage LM, Smith SA. Rapid, high-resolution quantitative magnetization transfer MRI of the human spinal cord. *Neuroimage*. 2014;95:106-116. doi:10.1016/j.neuroimage.2014.03.005
4. Smith AK, By S, Lyttle BD, et al. Evaluating single-point quantitative magnetization transfer in the cervical spinal cord: Application to multiple sclerosis. *NeuroImage Clin*. 2017;16:58-65. doi:10.1016/j.nicl.2017.07.010
5. Barkhof F. The clinico-radiological paradox in multiple sclerosis revisited. *Curr Opin Neurol*. 2002;15(3):239-245. doi:10.1097/00019052-200206000-00003
6. Zhou J, Payen J-F, Wilson DA, Traystman RJ, van Zijl PCM. Using the amide proton signals of intracellular proteins and peptides to detect pH effects in MRI. *Nat Med*. 2003;9:1085. https://doi.org/10.1038/nm907.
7. Dula AN, Gochberg DF, Valentine HL, Valentine WM, Does MD. Multiexponential T2, magnetization transfer, and Quantitative histology in white matter tracts of rat spinal cord. *Magn Reson Med*. 2010;63(4):902-909. doi:10.1002/mrm.22267
8. Wolff SD, Balaban RS. Magnetization transfer contrast (MTC) and tissue water proton relaxation in vivo. *Magn Reson Med*. 2018;10(1):135-144. doi:10.1002/mrm.1910100113
9. Zhou J, Wilson DA, Sun PZ, Klaus JA, van Zijl PCM. Quantitative description of proton exchange processes between water and endogenous and exogenous agents for WEX, CEST, and APT experiments. *Magn Reson Med*. 2004;51(5):945-952. doi:10.1002/mrm.20048
10. Henkelman RM, Stanisz GJ, Graham SJ. Magnetization transfer in MRI: A review. *NMR Biomed*. 2001;14(2):57-64. doi:10.1002/nbm.683
11. Kucharczyk W, Macdonald PM, Stanisz GJ, Henkelman RM. Relaxivity and magnetization transfer of white matter lipids at MR imaging: Importance of cerebrosides and pH. *Radiology*. 1994;192(2):521-529. doi:10.1148/radiology.192.2.8029426
12. Schmierer K, Tozer DJ, Scaravilli F, et al. Quantitative magnetization transfer imaging in postmortem multiple sclerosis brain. *J Magn Reson Imaging*. 2007;26(1):41-51. doi:10.1002/jmri.20984
13. Stanisz GJ, Odrobina EE, Pun J, et al. T1, T2 relaxation and magnetization transfer in tissue at 3T. *Magn Reson Med*. 2005;54(3):507-512. doi:10.1002/mrm.20605
14. Henkelman RM, Huang X, Xiang Q -S, Stanisz GJ, Swanson SD, Bronskill MJ. Quantitative interpretation of magnetization transfer. *Magn Reson Med*. 1993;29(6):759-766. doi:10.1002/mrm.1910290607
15. Berry I, Barker GJ, Barkhof F, et al. A multicenter measurement of magnetization transfer ratio in normal white matter. *J Magn Reson Imaging*. 1999;9(3):441-446. doi:10.1002/(SICI)1522-2586(199903)9:3<441::AID-JMRI12>3.0.CO;2-R

16. Sled JG, Pike GB. Quantitative imaging of magnetization transfer exchange and relaxation properties in vivo using MRI. *Magn Reson Med*. 2001;46(5):923-931. doi:10.1002/mrm.1278
17. Morrison C, Stanisz G, Henkelman RM. Modeling Magnetization Transfer for Biological-like Systems Using a Semi-solid Pool with a Super-Lorentzian Lineshape and Dipolar Reservoir. *J Magn Reson Ser B*. 1995;108(2):103-113. doi:10.1006/jmrb.1995.1111
18. Hinton DP, Bryant RG. 1H magnetic cross-relaxation between multiple solvent components and rotationally immobilized protein. *Magn Reson Med*. 1996;35(4):497-505. doi:10.1002/mrm.1910350408
19. Underhill HR, Yuan C, Yarnykh VL. Direct quantitative comparison between cross-relaxation imaging and diffusion tensor imaging of the human brain at 3.0 T. *Neuroimage*. 2009;47(4):1568-1578. doi:10.1016/j.neuroimage.2009.05.075
20. Yarnykh VL, Yuan C. Cross-relaxation imaging reveals detailed anatomy of white matter fiber tracts in the human brain. *Neuroimage*. 2004;23(1):409-424. doi:10.1016/j.neuroimage.2004.04.029
21. van Zijl PCM, Yadav NN. Chemical exchange saturation transfer (CEST): what is in a name and what isn't? *Magn Reson Med*. 2011;65(4):927-948. doi:10.1002/mrm.22761
22. Wu B, Warnock G, Zaiss M, et al. An overview of CEST MRI for non-MR physicists. *EJNMMI Phys*. 2016;3(1):19. doi:10.1186/s40658-016-0155-2
23. Zaiss M, Xu J, Goerke S, et al. Inverse Z-spectrum analysis for spillover-, MT-, and T1 -corrected steady-state pulsed CEST-MRI--application to pH-weighted MRI of acute stroke. *NMR Biomed*. 2014;27(3):240-252. doi:10.1002/nbm.3054
24. van Zijl PCM, Lam WW, Xu J, Knutsson L, Stanisz GJ. Magnetization Transfer Contrast and Chemical Exchange Saturation Transfer MRI. Features and analysis of the field-dependent saturation spectrum. *Neuroimage*. 2018;168:222-241. doi:10.1016/j.neuroimage.2017.04.045
25. Sherry AD, Woods M. Chemical Exchange Saturation Transfer Contrast Agents for Magnetic Resonance Imaging. *Annu Rev Biomed Eng*. 2008;10:391-411. doi:10.1146/annurev.bioeng.9.060906.151929
26. Zhou J, Payen JF, Wilson DA, Traystman RJ, Van Zijl PCM. Using the amide proton signals of intracellular proteins and peptides to detect pH effects in MRI. *Nat Med*. 2003;9(8):1085-1090. doi:10.1038/nm907
27. Guivel-Scharen V, Sinnwell T, Wolff SD, Balaban RS. Detection of Proton Chemical Exchange between Metabolites and Water in Biological Tissues. *J Magn Reson*. 1998;133(1):36-45. doi:10.1006/jmre.1998.1440
28. Hua J, Jones CK, Blakeley J, Smith SA, Van Zijl PCM, Zhou J. Quantitative description of the asymmetry in magnetization transfer effects around the water resonance in the human brain. *Magn Reson Med*. 2007;58(4):786-793. doi:10.1002/mrm.21387
29. Zu Z. Toward more reliable measurements of NOE effects in CEST spectra at around −1.6 ppm (NOE (−1.6)) in rat brain. *Magn Reson Med*. 2019;81(1):208-219. doi:10.1002/mrm.27370
30. Desmond KL, Stanisz GJ. Understanding quantitative pulsed CEST in the presence of MT. *Magn Reson Med*. 2012;67(4):979-990. doi:10.1002/mrm.23074
31. Sun PZ, van Zijl PCM, Zhou J. Optimization of the irradiation power in chemical exchange

dependent saturation transfer experiments. *J Magn Reson*. 2005;175(2):193-200. doi:10.1016/j.jmr.2005.04.005
32. Jin T, Autio J, Obata T, Kim SG. Spin-locking versus chemical exchange saturation transfer MRI for investigating chemical exchange process between water and labile metabolite protons. *Magn Reson Med*. 2011;65(5):1448-1460. doi:10.1002/mrm.22721
33. Jones CK, Polders D, Hua J, et al. In vivo three-dimensional whole-brain pulsed steady-state chemical exchange saturation transfer at 7 T. *Magn Reson Med*. 2012;67(6):1579-1589. doi:10.1002/mrm.23141
34. Zaiss M, Bachert P. Exchange-dependent relaxation in the rotating frame for slow and intermediate exchange - modeling off-resonant spin-lock and chemical exchange saturation transfer. *NMR Biomed*. 2013;26(5):507-518. doi:10.1002/nbm.2887
35. Kim M, Gillen J, Landman BA, Zhou J, Van Zijl PCM. Water saturation shift referencing (WASSR) for chemical exchange saturation transfer (CEST) experiments. *Magn Reson Med*. 2009;61(6):1441-1450. doi:10.1002/mrm.21873
36. Zaiss M, Windschuh J, Paech D, et al. Relaxation-compensated CEST-MRI of the human brain at 7 T: Unbiased insight into NOE and amide signal changes in human glioblastoma. *Neuroimage*. 2015;112:180-188. doi:10.1016/j.neuroimage.2015.02.040
37. Smith SA, Bulte JWM, Van Zijl PCM. Direct saturation MRI: Theory and application to imaging brain iron. *Magn Reson Med*. 2009;62(2):384-393. doi:10.1002/mrm.21980
38. Williams ML, Williams ML. The general solution to the bloch equation with constant rf and relaxation terms: Application to saturation and slice selection. *Med Phys*. 1993;20(1):5-13. doi:10.1118/1.597063
39. Zhang X-Y, Wang F, Li H, et al. Accuracy in the quantification of chemical exchange saturation transfer (CEST) and relayed nuclear Overhauser enhancement (rNOE) saturation transfer effects. *NMR Biomed*. 2017;30(7):e3716. doi:10.1002/nbm.3716
40. Yarnykh VL. Pulsed Z-spectroscopic imaging of cross-relaxation parameters in tissues for human MRI: Theory and clinical applications. *Magn Reson Med*. 2002;47(5):929-939. doi:10.1002/mrm.10120
41. Smith AK, Ray KJ, Larkin JR, Craig M, Smith SA, Chappell MA. Does the magnetization transfer effect bias chemical exchange saturation transfer effects? Quantifying chemical exchange saturation transfer in the presence of magnetization transfer. *Magn Reson Med*. February 2020:mrm.28212. doi:10.1002/mrm.28212
42. De Leener B, Levy S, Dupont SM, et al. SCT: Spinal Cord Toolbox, an open-source software for processing spinal cord MRI data. *Neuroimage*. 2017;145(Pt A):24-43. doi:10.1016/j.neuroimage.2016.10.009
43. Jones CK, Huang A, Xu J, et al. Nuclear Overhauser enhancement (NOE) imaging in the human brain at 7T. *Neuroimage*. 2013;77:114-124. doi:10.1016/j.neuroimage.2013.03.047
44. Jin T, Wang P, Zong X, Kim SG. MR imaging of the amide-proton transfer effect and the pH-insensitive nuclear overhauser effect at 9.4 T. *Magn Reson Med*. 2013;69(3):760-770. doi:10.1002/mrm.24315
45. Zaiß M, Schmitt B, Bachert P. Quantitative separation of CEST effect from magnetization transfer and spillover effects by Lorentzian-line-fit analysis of z-spectra. *J Magn Reson*. 2011;211(2):149-155. doi:10.1016/j.jmr.2011.05.001

46. Singh A, Debnath A, Cai K, et al. Evaluating the feasibility of creatine-weighted CEST MRI in human brain at 7 T using a Z-spectral fitting approach. *NMR Biomed*. 2019;32(12). doi:10.1002/nbm.4176
47. Hua J, Jones CK, Blakeley J, Smith SA, van Zijl PCM, Zhou J. Quantitative description of the asymmetry in magnetization transfer effects around the water resonance in the human brain. *Magn Reson Med*. 2007;58(4):786-793. doi:10.1002/mrm.21387
48. McMahon MT, Gilad AA, Zhou J, Sun PZ, Bulte JWM, van Zijl PCM. Quantifying exchange rates in chemical exchange saturation transfer agents using the saturation time and saturation power dependencies of the magnetization transfer effect on the magnetic resonance imaging signal (QUEST and QUESP): Ph calibration for poly. *Magn Reson Med*. 2006;55(4):836-847. doi:10.1002/mrm.20818
49. Mehrabian H, Lam WW, Myrehaug S, Sahgal A, Stanisz GJ. Glioblastoma (GBM) effects on quantitative MRI of contralateral normal appearing white matter. *J Neurooncol*. 2018;139(1):97-106. doi:10.1007/s11060-018-2846-0
50. Heo HY, Zhang Y, Lee DH, Hong X, Zhou J. Quantitative assessment of amide proton transfer (APT) and nuclear overhauser enhancement (NOE) imaging with extrapolated semi-solid magnetization transfer reference (EMR) signals: Application to a rat glioma model at 4.7 tesla. *Magn Reson Med*. 2016;75(1):137-149. doi:10.1002/mrm.25581
51. Mehrabian H, Myrehaug S, Soliman H, Sahgal A, Stanisz GJ. Quantitative Magnetization Transfer in Monitoring Glioblastoma (GBM) Response to Therapy. *Sci Rep*. 2018;8(1):1-11. doi:10.1038/s41598-018-20624-6
52. Goldenberg MM. Multiple sclerosis review. *P T*. 2012;37(3):175-184. https://www.ncbi.nlm.nih.gov/pubmed/22605909.
53. KURTZKE JF. Disability Rating Scales in Multiple Sclerosis. *Ann N Y Acad Sci*. 2018;436(1):347-360. doi:10.1111/j.1749-6632.1984.tb14805.x
54. Kuceyeski AF, Vargas W, Dayan M, et al. Modeling the relationship among gray matter atrophy, abnormalities in connecting white matter, and cognitive performance in early multiple sclerosis. In: *American Journal of Neuroradiology*. Vol 36. American Society of Neuroradiology; 2015:702-709. doi:10.3174/ajnr.A4165
55. Popescu BFG, Pirko I, Lucchinetti CF. Pathology of Multiple Sclerosis: Where Do We Stand? *Contin Lifelong Learn Neurol*. 2013;19(4 Multiple Sclerosis):901-921. doi:10.1212/01.CON.0000433291.23091.65
56. PS G, IR L, Ribeiro L, al et. Measuring demyelination and remyelination in acute multiple sclerosis lesion voxels. *Arch Neurol*. 2009;66(3):375-381. http://dx.doi.org/10.1001/archneurol.2008.578.
57. Thompson AJ, Banwell BL, Barkhof F, et al. Diagnosis of multiple sclerosis: 2017 revisions of the McDonald criteria. *Lancet Neurol*. 2018;17(2):162-173. doi:10.1016/S1474-4422(17)30470-2
58. Rammohan KW. Cerebrospinal fluid in multiple sclerosis. *Ann Indian Acad Neurol*. 2009;12(4):246-253. doi:10.4103/0972-2327.58282
59. Tintore M, Rovira A, Rio J, et al. Do oligoclonal bands add information to MRI in first attacks of multiple sclerosis? *Neurology*. 2008;70(13 Pt 2):1079-1083. doi:10.1212/01.wnl.0000280576.73609.c6
60. Whitaker JN, Gupta M, Smith OF. Epitopes of immunoreactive myelin basic protein in

human cerebrospinal fluid. *Ann Neurol*. 1986;20(3):329-336. doi:10.1002/ana.410200310
61. Ohta M, Ohta K. Detection of myelin basic protein in cerebrospinal fluid. *Expert Rev Mol Diagn*. 2002;2(6):627-633. doi:10.1586/14737159.2.6.627
62. Waldman AT, Stull LB, Galetta SL, Balcer LJ, Liu GT. Pediatric optic neuritis and risk of multiple sclerosis: Meta-analysis of observational studies. *J Am Assoc Pediatr Ophthalmol Strabismus {JAAPOS}*. 2011;15(5):441-446. doi:10.1016/j.jaapos.2011.05.020
63. Lisanti C, Carlin C, Banks KP, Wang D. Normal MRI Appearance and Motion-Related Phenomena of CSF. *Am J Roentgenol*. 2007;188(3):716-725. doi:10.2214/AJR.05.0003
64. Whitaker JN. Myelin basic protein and multiple sclerosis. *Ital J Neurol Sci*. 1983;4(2):153-157.
65. Comabella M, Montalban X. Body fluid biomarkers in multiple sclerosis. *Lancet Neurol*. 2014;13(1):113-126. doi:10.1016/S1474-4422(13)70233-3